

**The Thermochemistry of
Protonated and Sodiated Clusters
Investigated *via* High-Pressure Mass Spectrometry**

by

Matthew Aaron Furzeczott

A thesis

presented to the University of Waterloo

in fulfilment of the thesis

requirement for the degree of

Master of Science

in

Chemistry

Waterloo, Ontario Canada, 2007

© Matthew Aaron Furzeczott 2007

I hereby declare that I am the sole author of this thesis. This is a true copy of the thesis, including any required final revisions, as accepted by my examiners.

I understand that my thesis may be made electronically available to the public.

Abstract

High-pressure mass spectrometry has been employed to investigate hydrogen and sodium bound ion-molecule complexes in the gas phase. Insight into the structure and reactivity of ion-molecule complexes has been gained by examining simple mono-ketones of butanone and 2-pentanone and more complex β -diketones of 2,4-pentanedione, 1,1,1-trifluoro-2,4-pentanedione and 1,1,1,5,5,5-hexafluoro-2,4-pentanedione. The effect of fluorinating 2,4-pentanedione exhibits experimental trends that are not representative of current electronic structure calculations .

A novel method of sodium ion production has been developed using sodium metal, allowing for equilibrium measurements below 150 °C. Sodium containing ion-molecule complexes have been investigated using the new method of sodium ion production.

Acknowledgments

I would like to thank my supervisor, Terry, for all his help and encouragement throughout my time here at The University of Waterloo. I am also very grateful to Terry for the opportunity to work in his lab with him as a graduate student. The research was interesting, exciting and at times somewhat frustrating, but overall an excellent experience that I would trade nothing for. Thanks for everything Terry.

The McMahon research group has always been very helpful, supportive and entertaining throughout my time here and I would like to express my gratitude to them. I would like to thank Ronghu for his helpful insight into experimental problems (which helped me on a number of occasions) and his friendly nature, always willing to stop and chat about research and non-research topics alike. Rick, Rob, Kris, Jon thanks for all the help and good times these past few years. I appreciate all the knowledge you have imparted on me and all the help with experimental and theoretical problems encountered. Thanks to all of you for making the time spent in the lab, outside of the lab and at the many conferences we attended a great time.

I would also like to thank Travis Fridgen for his guidance during my days as an undergraduate and my early days as a graduate student. I would like to thank Travis for introducing me to the McMahon group and his constant encouragement in my endeavours.

Lastly, I would like to thank my friends and family, especially my parents, for their support throughout these years. At times I have been mildly distracted and at others I have been completely missing-in-action and I want to thank my friends and family for their constant understanding and encouragement.

Table of Contents

1.0	Introduction.....	1
1.1	High-Pressure Mass Spectrometry.....	3
1.2	Ion Formation in the HPMS System.....	3
1.3	The VG-7070 HPMS of Reverse (BE) Geometry	6
1.4	Determination of Thermochemistry using HPMS	10
1.5	Determination of Equilibrium.....	14
1.6	Computational Methods.....	20
2.0	Sample Preparation – Sodium.....	24
2.1	Sodium Sample Container	25
2.2	The Top Hat	26
2.3	The Glass Ampoule.....	28
2.4	The Stainless Steel Boat.....	31
3.0	Proton Bound Dimers	33
3.1	Introduction to Proton Bound Dimer Systems.....	33
3.2	Butanone	37
3.3	2-Pentanone	42
3.4	2,4-Pentanedione System.....	48
3.5	1,1,1-Trifluoro 2,4 pentanedione system	58
3.6	1,1,1,5,5,5-Hexafluoro-2,4-Pentanedione System	63
3.7	Conclusion	71
4.0	Sodiated Clusters	73
4.1	Introduction to Sodiated Clusters.....	73
4.2	Diethylether Results and Discussion.....	75
4.3	THF Results and Discussion.....	79
4.31	Na-THF ⁺ Measurement.....	79
4.32	THF PBD Measurement	83
4.4	Conclusion	86
5.0	References.....	87

Table of Figures

FIGURE 1	THE VG-7070 MASS SPECTROMETER CONVERTED TO REVERSE GEOMETRY EQUIPPED WITH A HIGH-PRESSURE ION SOURCE AND COLLISION CELL	6
FIGURE 2	SCHEMATIC OF THE VG-7070 SHOWING THE HIGH-PRESSURE REGION	8
FIGURE 3	TIME-INTENSITY PROFILE	16
FIGURE 4	LOGARITHMIC TIME-INTENSITY PROFILE.....	17
FIGURE 5	NORMALIZED TIME-INTENSITY PROFILE.....	19
FIGURE 6	STAINLESS STEEL TOP HAT.....	26
FIGURE 7	ION SOURCE WITH HEATING JACKET.....	27
FIGURE 8	GLASS AMPOULE WITH CAGE AND SODIUM SEPARATE	29
FIGURE 9	GLASS AMPOULE IN CAGE (SODIUM NOT VISIBLE)	29
FIGURE 10	THE STAINLESS STEEL BOAT	31
FIGURE 11	INTERMOLECULAR HYDROGEN BOND	34
FIGURE 12	INTRAMOLECULAR HYDROGEN BOND.....	34
FIGURE 13	IONIC HYDROGEN BOND.....	35
FIGURE 14	VAN'T HOFF PLOT OF BUTANONE.....	39
FIGURE 15	THE MP2/6-311++G(3DF,3PD)// B3LYP/6-311++G(3DF,3PD) OPTIMIZED REPRESENTATION OF THE BUTANONE PBD FORMATION.....	41
FIGURE 16	VAN'T HOFF PLOT OF 2-PENTANONE	44
FIGURE 17	THE G3(MP2) OPTIMIZED REPRESENTATION OF THE 2-PENTANONE PBD FORMATION	46
FIGURE 18	VAN'T HOFF PLOT OF 2,4-PENTANEDIONE.....	49
FIGURE 19	G3(MP2) OPTIMIZED STRUCTURES OF THE KETO-ENOL EQUILIBRIUM OF 2,4-PENTANEDIONE	50
FIGURE 20	G3(MP2) OPTIMIZED STRUCTURES OF THE KETO-ENOL EQUILIBRIUM OF PROTONATED 2,4-PENTANEDIONE.....	52
FIGURE 21	MP2(FULL)/6-311+G(D,P)//MP2(FULL)6-311G(D) OPTIMIZED STRUCTURES OF THE PBD OF 2,4-PENTANEDIONE.....	53
FIGURE 22	REACTION SCHEME A1- ENOL-ENOL PBD OF 2,4-PENTANEDIONE	55
FIGURE 23	REACTION SCHEME A2 - KETO-ENOL PBD OF 2,4-PENTANEDIONE	55
FIGURE 24	REACTION SCHEME A3 – KETO-ENOL PBD OF 2,4-PENTANEDIONE.....	55

FIGURE 25	VAN'T HOFF PLOT OF 1,1,1-TRIFLUORO-2,4-PENTANEDIONE	59
FIGURE 26	KETO-ENOL EQUILIBRIUM OF 1,1,1-TRIFLUORO-2,4-PENTANEDIONE	60
FIGURE 27	KETO-ENOL EQUILIBRIUM OF PROTONATED 1,1,1-TRIFLUORO-2,4-PENTANEDIONE	61
FIGURE 28	MOST LIKELY PBD FORMATION OF 1,1,1-TRIFLUORO-2,4-PENTANEDIONE AS CALCULATED BY B3LYP/6-311++G(2DF,2PD)//B3LYP/6-31G(D)	62
FIGURE 29	VAN'T HOFF PLOT OF 1,1,1,5,5,5-HEXAFLUORO-2,4-PENTANEDIONE	65
FIGURE 30	KETO-ENOL EQUILIBRIUM OF PROTONATED 1,1,1,5,5,5-HEXAFLUORO-2,4-PENTANEDIONE	66
FIGURE 32	MOST LIKELY PBD FORMATION OF 1,1,1,5,5,5-HEXAFLUORO-2,4-PENTANEDIONE AS CALCULATED BY MP2(FULL)/6-311+G(D,P)//B3LYP/6-31G(D)	66
FIGURE 33	REACTION SCHEME B1 FOR 1,1,1,5,5,5-HEXAFLUORO-2,4-PENTANEDIONE	68
FIGURE 34	REACTION SCHEME B2 FOR 1,1,1,5,5,5-HEXAFLUORO-2,4-PENTANEDIONE	68
FIGURE 35	REACTION SCHEME B3 FOR 1,1,1,5,5,5-HEXAFLUORO-2,4-PENTANEDIONE	68
FIGURE 36	POSSIBLE COVALENT STRUCTURE OF 1,1,1,5,5,5-HEXAFLUORO-2,4-PENTANEDIONE	70
FIGURE 37	VAN'T HOFF PLOT OF $\text{Na-Et}_2\text{O}^+$	76
FIGURE 38	THE B3LYP/6-311+G(D,P) OPTIMIZED STRUCTURE OF $\text{Na-Et}_2\text{O}^+$ FORMATION	77
FIGURE 39	VAN'T HOFF PLOT OF Na-THF^+ FORMATION	81
FIGURE 40	THE G3(MP2) OPTIMIZED STRUCTURE OF Na-THF^+ FORMATION	82
FIGURE 41	VAN'T HOFF PLOT OF THF PBD FORMATION	84
FIGURE 42	THE G3(MP2) OPTIMIZED STRUCTURE OF THF PBD FORMATION	85

Table of Tables

TABLE 1	A DETAILED COMPONENT LIST FOR THE MODIFIED VG-7070 AT THE UNIVERSITY OF WATERLOO (FIGURE 1)	7
TABLE 2	BOILING POINTS SUMMARY OF SIMPLE OXYGEN CONTAINING SPECIES	33
TABLE 3	BUTANONE THERMOCHEMICAL DATA, EXPERIMENTAL AND CALCULATED SUMMARY	40
TABLE 4	2-PENTANONE THERMOCHEMICAL DATA, EXPERIMENTAL AND CALCULATED SUMMARY	45
TABLE 5	2,4-PENTANEDIONE THERMOCHEMICAL DATA, EXPERIMENTAL AND CALCULATED SUMMARY	56
TABLE 6	1,1,1-TRIFLUORO-2,4-PENTANEDIONE THERMOCHEMICAL DATA, EXPERIMENTAL AND CALCULATED SUMMARY	62
TABLE 7	1,1,1,5,5,5-HEXAFLUORO-2,4-PENTANEDIONE THERMOCHEMICAL DATA, EXPERIMENTAL AND CALCULATED SUMMARY	67
TABLE 8	SUMMARY OF REACTION SCHEMES B1-B3 FOR 1,1,1,5,5,5,HEXAFLUORO-2,4-PENTANEDIONE	69
TABLE 9	NA-ET ₂ O ⁺ THERMOCHEMICAL DATA, EXPERIMENTAL AND CALCULATED SUMMARY	77
TABLE 10	NA-THF ⁺ THERMOCHEMICAL DATA, EXPERIMENTAL AND CALCULATED SUMMARY	82
TABLE 11	THF PBD THERMOCHEMICAL DATA, EXPERIMENTAL AND CALCULATED SUMMARY	85

List of Acronyms, Symbols and Constants

NIST – National Institute of Standards and Technology
HPMS – High-Pressure Mass Spectrometry
PBD – Proton Bound Dimer
CI – Chemical Ionization
Eq. – Equation
atm - Atmosphere
o.d. – Outer Diameter
i.d. – Inner Diameter
ca. – Circa
CID – Collision Induced Dissociation
LID – Laser Induced Dissociation
MIKES – Mass (analyzed) Ion Kinetic Energy Spectroscopy
MCS – Multi-Channel Scalar
ESA – Electrostatic Analyzer
n.i. – Normalized Intensity
HF – Hartree-Fock
SCF – Self-Consistent Field
MP – Møller-Plesset
DFT – Density Functional Theory
B3LYP – Becke 3-Parameter Exchange, Lee, Yang, Parr
SHARCNET - Shared Hierarchical Academic Research Network
 K_{eq} – Equilibrium Constant
 ΔH° - Standard Enthalpy Change
 ΔS° - Standard Entropy Change
 ΔG° - Standard Gibbs Free Energy Change
 P_A – Partial Pressure
 R – Universal Gas Constant
IHB – Ionic Hydrogen Bond
 m/z – Mass-to-Charge
SCA – Sodium Cation Affinity
FT-ICR-MS – Fourier Transform Ion Cyclotron Resonance Mass Spectrometry
 Et_2O – Diethylether
THF - Tetrahydrofuran

1.0 Introduction

Applications of gas phase ion-molecule interactions are diverse. The area of gas phase ion-molecule chemistry can be applied to all aspects of life, from probing the intimate details of the structure and reactivity of small molecules, to exploring biological processes involving many molecules, to astrophysical experiments investigating the origins of life on earth.¹⁻³ As the implications of the results of these studies are extensive and influential, considerable attention has been directed towards the collection and evaluation of gas phase ion-molecule data.

For the past 50 years the collection of gas phase ion-molecule energetics has been under constant review. The origins of the series of publications devoted to this subject area can be traced to the 1957 book titled “Electron Impact Phenomena and the Properties of Gaseous Ions” by F. H. Field and J. L. Franklin.⁴ Gas phase ion-molecule interactions are studied using a wide variety of experimental techniques. Since the beginnings of the investigations of ion energetic data, continual updates have been published. The current form of the publications is a WebBook published by the National Institute of Standards and Technology (NIST).⁴ The NIST WebBook is an online searchable database of ionization energies, appearance energies, proton affinities, electron affinities, gas phase acidities and basicities and ion-molecule thermochemical values, among other properties.

The study of gas phase ion-molecule chemistry has exploded in the past 50 years due to the wide range of unique environments that can be achieved. Developments in spectrometric and spectroscopic methods continue to expand the range of ion-molecule systems that can be investigated. These unique environments permit observations of ion-molecule complexes that not only vary in size but vary in the chemistry that can be explored. One such unique environment is encountered in high-pressure mass spectrometry (HPMS).

High-pressure mass spectrometry is a direct result of the type of technique development that has fuelled research in gas phase ion chemistry for the past 50 years. The original intent was to replicate the environment in which radiolysis experiments were carried out.⁵ Although application of these high-pressure techniques to the radiolysis experiments proved unsatisfactory, another interesting discovery was made. The observation of multiply solvated protons dominated the mass spectrum.⁵ This observation led to the realization that successive solvation equilibria could be studied. The technique of high-pressure mass spectrometry was originally pioneered by Paul Kebarle and co-workers at the University of Alberta in the early 1960's.⁶ Since the inception of HPMS, the technique has proven to be a valuable tool used to study the approach to, and attainment of equilibrium⁷⁻⁹ and a wide variety of investigations have been carried out. HPMS has been used to study ion-ligand and ion-solvent equilibria, gas phase acidities and basicities, proton transfer, electron affinities, ionization energies, among many other processes.¹⁰ The technique of HPMS continues to evolve. Developments in the method of sample introduction continue to expand the range of compounds that can be studied using the HPMS technique.¹¹ The objective of this thesis is to contribute to these databases by providing fundamental thermochemical information to aid in the understanding of all systems chemical.

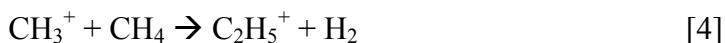
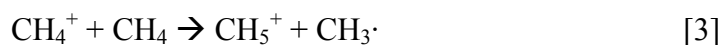
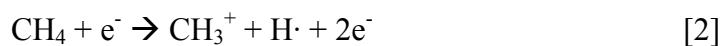
1.1 High-Pressure Mass Spectrometry

To obtain thermochemical information using mass spectrometry, all species must be in chemical and thermal equilibrium. These conditions are met using the high-pressure mass spectrometry technique.^{5,6,12} The unique high-pressure mass spectrometer provides an environment suitable for the measurement of equilibrium constants as a function of temperature. The equilibrium constant determination will be discussed in Section 1.4. By studying the equilibrium constant of association reactions as a function of temperature, van't Hoff plots can be generated, which allow the thermochemical values to be obtained for a reaction. Details of how this is achieved are given below.

1.2 Ion Formation in the HPMS System

HPMS involves the use of an ion source pressure of ≥ 5 torr which makes it unique relative to conventional forms of mass spectrometry which operate with ion source pressures considerably lower ($\leq 10^{-4}$ torr). Unique to the HPMS instrument at the University of Waterloo is the incorporation of a very high pumping speed (5300 L s^{-1}) diffusion pump on the source housing which permits ion source pressures up to 50 torr to be used.¹² With pressures of this magnitude, ions undergo 10^6 - 10^7 stabilizing collisions with the predominant bath gas before exiting from the ion source, thus ensuring thermochemical equilibrium. The bath gas is usually a non-reactive species such as nitrogen, methane or argon which provides collisional stabilization and also acts as a chemical ionization (CI) agent. The ion-molecule collisions that occur in the source ensure that the ions have a true thermal Boltzmann distribution of kinetic and thermal energies characteristic of the temperature at which the ions are formed.¹²

In the following experiments both nitrogen and methane are used as bath gases. Methane is used as the bath gas for creating proton bound dimers (PBDs) while nitrogen is used to generate sodiated clusters. Methane is used as the bath gas for the formation of PBDs due to the inherent ability of a series of CI processes to readily protonate most species and its ability to act as a relatively inert third-body collisional agent. Nitrogen is used for the sodiated clusters as it provides efficient CI through charge transfer pathways. The CI reaction scheme is initiated by a pulsed-source of high energy (2000 eV) electrons. The methane CI reaction scheme is presented below through Equations (Eq.) 1-4.



In the PBD systems, ionization is achieved predominately through proton transfer from the CH_5^+ and C_2H_5^+ species. Protonated methane (CH_5^+) is a hyper-valent species while protonated ethene (C_2H_5^+) is a symmetric π -bonded species. Both are termed super-acidic as they readily donate a proton.¹³ The super-acidic species then transfer the acidic proton to the species of interest or analyte (A).



The analyte is protonated, (AH^+), and can then undergo association with the neutral analyte (A) forming the PBD, AHA^+ .

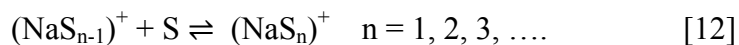
In the sodiated experiments nitrogen is used as the bath gas. Nitrogen is used as a CI agent since it is relatively inert and provides a suitable gas for ionization of sodium vapour *via* charge transfer. Nitrogen is also used to suppress PBD formation by denying a significant source of protons which are necessary for PBD formation. A reaction scheme involving nitrogen as the bath gas and sodium as the species being ionized is shown in Eq. 8-10. Again ionization occurs *via* the collision of high energy (2 keV) electrons with N_2 .



The sodium cation can undergo stabilization *via* third body collision with the neutral nitrogen molecules. The sodium ions then cluster with the solvent molecules (S) present in the system (Eq. 11-12).



or



1.3 The VG-7070 HPMS of Reverse (BE) Geometry

The home-built HPMS used in this study employs a modified VG-7070 double focusing mass spectrometer as the mass analysis stage and is shown schematically below in Figure 1. A description of the components is given in Table 1. This particular HPMS has been described in detail previously¹⁴ so only the major modifications will be described here.

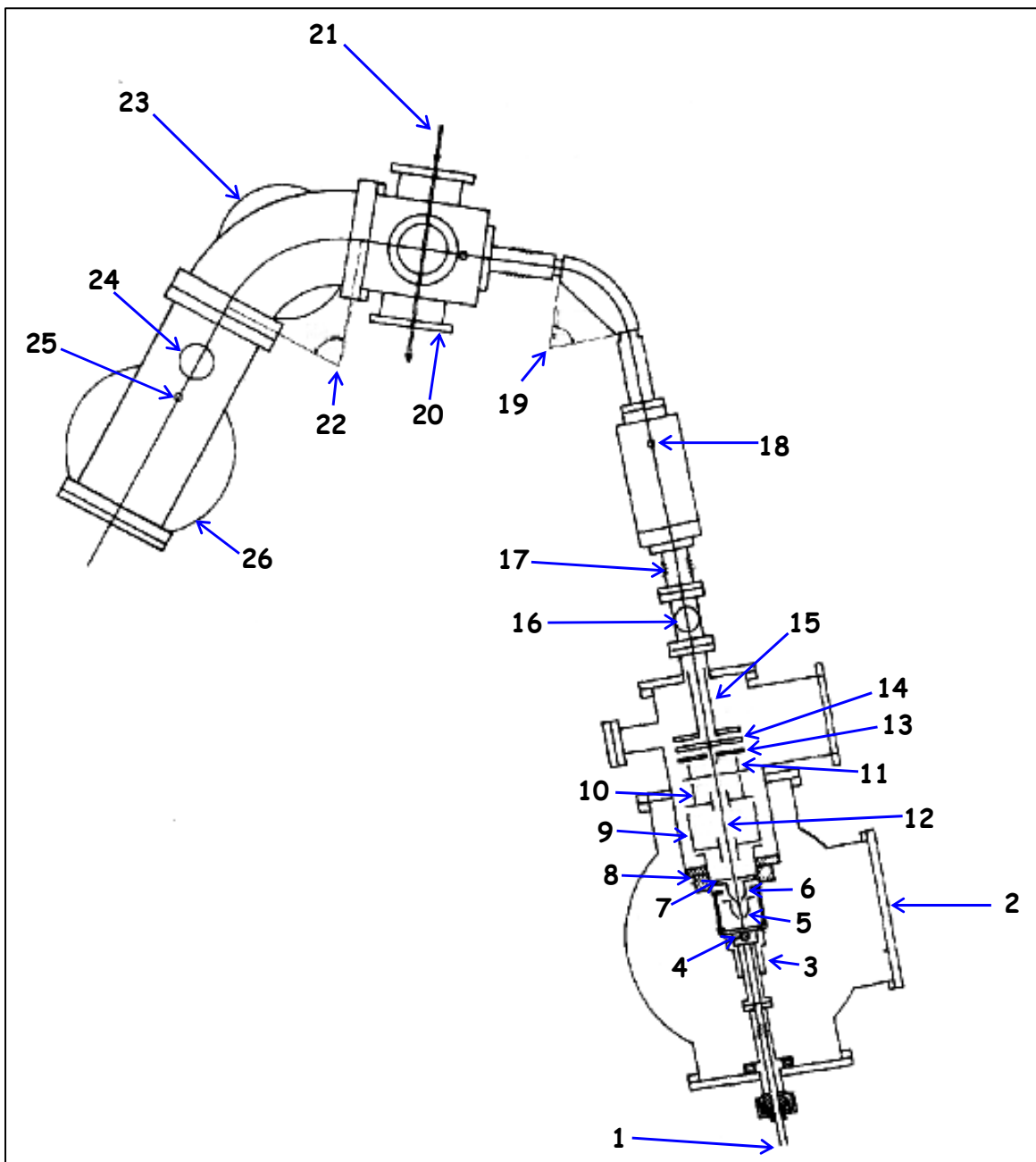


Figure 1 The VG-7070 Mass Spectrometer Converted to Reverse Geometry Equipped With a High-Pressure Ion Source and Collision Cell

Table 1 A Detailed Component List for the Modified VG-7070 at the University of Waterloo (Figure 1)

COMPONENT	DESCRIPTION OF COMPONENT
1	Gas sample inlet
2	Viewing port
3	Ion source block
4	Ion beam entrance aperture (200 μm)
5	First cone
6	Second cone
7	Top hat
8	Teflon support and sealing plug
9	First Einzel lens
10	Second Einzel lens
11	Third Einzel lens
12	Ion beam flight path
13	y-deflectors
14	z-deflectors
15	Shielding tunnel
16	Isolation valve
17	Bellows
18	First resolving slit
19	Magnetic sector (70° with radius of 12.7 cm)
20	Collision cell housing
21	Laser beam (optional photodissociation)
22	Electrostatic sector analyzer (70° with radius of 20.0 cm)
23	Edwards Diffusion Pump
24	Isolation valve
25	Final resolving slit
26	Collector housing and Edwards 63M Diffstak

An important modification of the VG-7070 mass spectrometer is the reversal of the direction of ion travel to produce a reverse geometry device. The substitution of the high-pressure source for that of the commercial unit along with the addition of a collision cell are two other important modifications. The high-pressure source is located in an Allaria vacuum chamber pumped by a Varian VHS 5300 L s⁻¹ vacuum pump (see Figure 2).

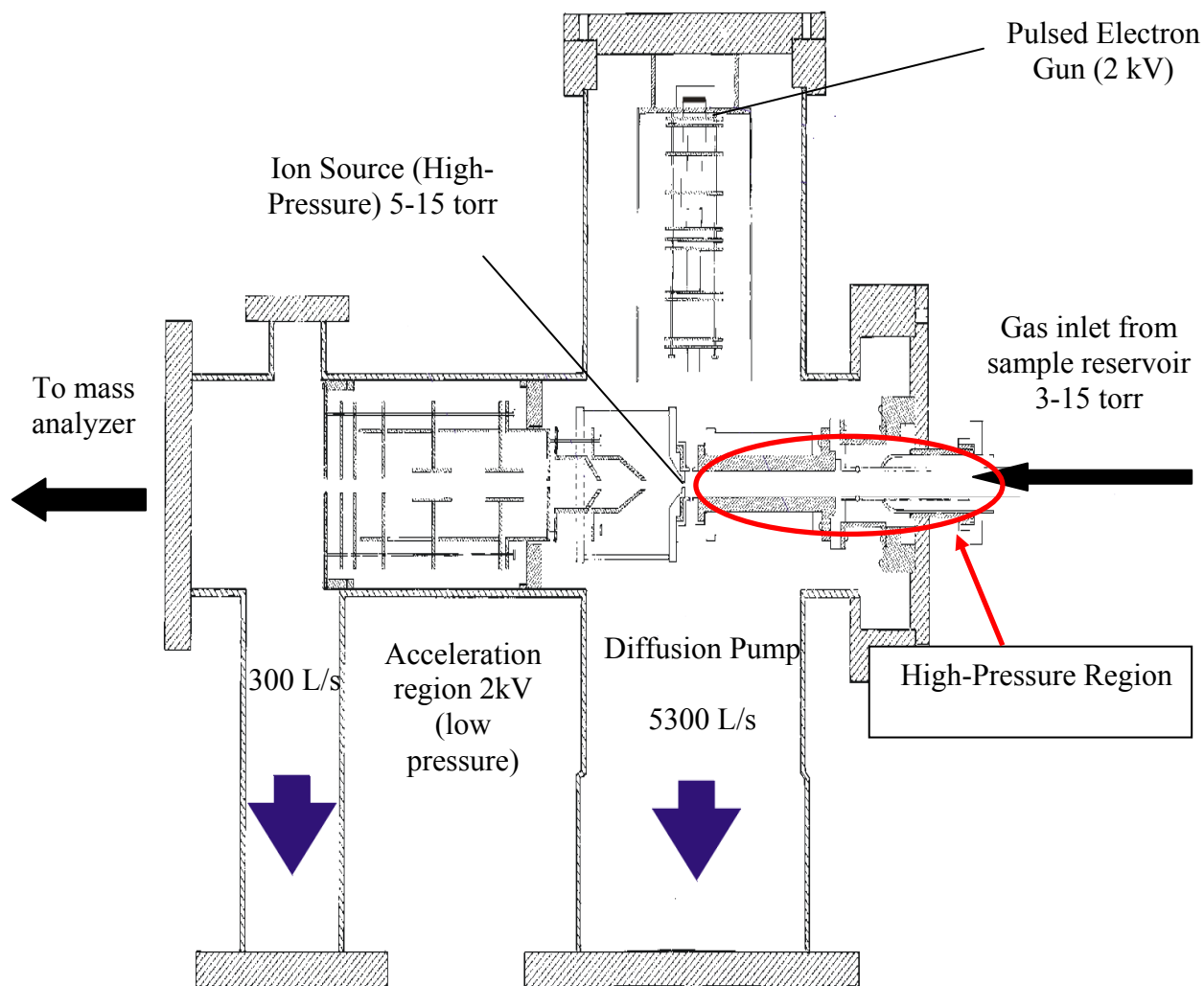


Figure 2 Schematic of the VG-7070 Showing the High-Pressure Region

The liquid sample mixtures are injected into a heated and calibrated 5 L reservoir containing ≈ 1 atm of bath gas prior to introduction to the ion source. This volatilizes the liquid samples creating the solvent gas. The sample mixture (solvent gas and bath gas) flows into the ion source from the reservoir through a heated inlet line.

The ion source block is cylindrical in shape (25 mm o.d., 13 mm i.d. and 200 mm long) and made of non-magnetic stainless steel. The block is surrounded by 8 cartridge heaters, used to provide reaction temperatures up to a maximum of ca. 500 °C. The source block contains two platinum-iridium apertures (200 μm) orthogonal to one another. The top (or entrance) aperture allows the high-energy (2 keV) electrons into the ion source block and the side (or exit) aperture allows ionized species to effuse out. Once the ions effuse out of the source they are accelerated by the ion optics where they can be transmitted through the mass analyzer and onto the detector. The temperature of the source block and the reaction chamber is measured *via* two iron-constantan thermocouples of the J-type, accurate to ± 1 degree, which are embedded in the source block surrounded by the cartridge heaters. The source and position of the sodium sample will be discussed in Section 2.0. The source of electrons is an electron gun modeled after a cathode ray tube of a television set. The electron gun is triggered by a pulse generator allowing for pulsed ionization experiments to be performed. Deflection electrodes and an Einzel lens system focus and accelerate the electrons onto the entrance aperture of the ion source. Once the electrons enter the ion source chemical ionization is initiated (Eq. 1-12). The ions produced effuse from the ion source where they are accelerated and focused by a set of skimmer cones, Einzel lens and deflectors onto the entrance slit of the magnetic sector of the mass spectrometer.

The second major modification of the VG-7070 is the addition of a collision cell immediately after the mass selector. The collision cell operates in a field-free region allowing for

collision-induced dissociation (CID), laser induced dissociation (LID) or unimolecular dissociation experiments to be carried out on ions of selected masses. The BE geometry also allows for mass (selected) ion kinetic energy spectra (MIKES) to be generated.

The VG-7070 mass spectrometer employs a 70 ° single magnetic sector mass analyzer with a 70 ° electrostatic analyzer (ESA). Fixing the magnetic field at particular values and permitting ions of all kinetic energies to pass the ESA allows ions of only a single mass to transit the radial path of the flight tube and strike the detector.

1.4 Determination of Thermochemistry using HPMS

The change in enthalpy, ΔH_{rxn}° , provides a quantitative measure of the strength of the noncovalent bond of the type shown below in Eq. 13,



where M^+ is a metal ion, L an electronegative atom containing molecule, and ML^+ is an ion-molecule complex.

To determine the thermochemistry of this reaction it is desirable to study the equilibrium constant of the clustering reaction over a relatively large temperature range. The experimental change in enthalpy and entropy can then be determined. The following will discuss the relationships between ΔH_{rxn}° and ΔS_{rxn}° and temperature.

A van't Hoff plot is a plot of the natural logarithm of the equilibrium constant versus the inverse of the temperature ($1/T$). This plot has a slope which is proportional to ΔH_{rxn}° and an intercept that is proportional to ΔS_{rxn}° . In order to obtain the van't Hoff expression two important thermodynamic relationships (Eq. 14 and 15) must be recalled.

$$\ln K_{eq} = -\frac{\Delta G_{rxn}^o}{RT} \quad [14]$$

$$\Delta G_{rxn}^o = \Delta H_{rxn}^o - T\Delta S_{rxn}^o \quad [15]$$

Substitution of ΔG_{rxn}^o from Eq. 15 into Eq. 14 yields the typical van't Hoff expression (Eq. 16).

$$\ln K_{eq} = -\frac{\Delta H_{rxn}^o}{R \cdot T} + \frac{\Delta S_{rxn}^o}{R} \quad [16]$$

A van't Hoff plot ($\ln K_{eq}$ vs $1/T$) gives a linear plot, if ΔH_{rxn}^o and ΔS_{rxn}^o are constant over the temperature range studied. From Eq. 16 a van't Hoff plot yields a slope given by Eq. 17 and an intercept given by Eq. 18.

$$\text{slope} = -\frac{\Delta H_{rxn}^o}{R} \quad [17]$$

$$\text{intercept} = \frac{\Delta S_{rxn}^o}{R} \quad [18]$$

The equilibrium reaction seen in Eq. 13 has an associated equilibrium constant (K_{eq}), given by Eq. 19,

$$K_{eq} = \frac{a_{ML^+}}{a_{M^+} a_L} \quad [19]$$

where a_i is the activity of the corresponding species.

To determine experimentally the equilibrium constant the activities must be measured. For dilute gases, the activity is equal to P/P_0 , where P is the partial pressure of the individual

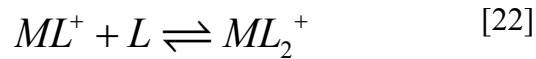
species and P_0 is the standard reference pressure and is equal to 1 bar. Substitution of these quantities into Eq. 19 gives Eq. 20.

$$K_{eq} = \frac{\frac{P_{ML^+}}{P_0}}{\frac{P_{M^+}}{P_0} \frac{P_L}{P_0}} \quad [20]$$

Rearranging Eq. 20 yields Eq. 21

$$K_{eq} = \frac{P_{ML^+}}{P_{M^+} P_L} P_0 \quad [21]$$

Using HPMS it is possible to obtain the ratio of the intensities of monomer and dimer cluster ions generated from the association reactions between the metal ions and the ligands or solvent molecules (Eq. 13). There are also higher order clusters of ions possible, as illustrated below in Eq. 22-24.



The intensity of the signal is directly proportional to the number of ions produced, which is directly proportional to the partial pressure of the ions. Therefore the partial pressure of a given ion can be equated to its intensity (Eq. 25).

$$P_i = k_i I_i \quad [25]$$

Where k_i is a proportionality constant and I_i is the intensity of the i^{th} ionic species. If the k_i 's of the reactant ion and product ion are assumed to be the same then the ratio of ion pressures can be equated to the intensities of the ions through Eq. 26.

$$\frac{P_{ML^+}}{P_{M^+}} = \frac{I_{ML^+}}{I_{M^+}} \quad [26]$$

Substituting Eq. 26 into Eq. 21, yields Eq. 27.

$$K_{eq} = \frac{I_{ML^+}}{I_{M^+} P_L} P_0 \quad [27]$$

By accurately knowing the partial pressure of the neutral solvent gas in the system (P_L), and by collection of ion intensity for M^+ and ML^+ (I_{M^+} and I_{ML^+}), it is possible to obtain an experimental equilibrium constant at a given temperature for a clustering reaction as shown by Eq. 13 and 22-24. From the injected volume, the molecular weight and the density, as well as the volume and temperature of the reservoir containing the solvent, P_L is determined using the ideal gas law (Eq. 28).

$$P_L V_L = n_L R T_{res} \quad [28]$$

In Eq 28 P_L is the partial pressure of the ligand, V_L is the injected volume of the ligand, n_L is the number of moles of ligand as determined by the density and volume, R is the universal gas constant ($8.3145 \text{ J mol}^{-1} \text{ K}^{-1}$) and T_{res} is the temperature of the reservoir.

Similarly, the equivalent expressions can be derived for proton bound dimer formation (Eq. 29)



The corresponding equilibrium constant expression is:

$$K_{eq} = \frac{I_{AHA^+}}{I_{AH^+} P_A} P_0 \quad [30]$$

where P_A is the partial pressure of the solvent gas, I_{AHA^+} is the intensity of the PBD ion, I_{AH^+} is the intensity of the protonated monomer and P_0 is the reference pressure of 1 bar.

The amount of clustering gas (solvent gas) in the reservoir is typically < 1% of the total gas mixture. Nitrogen, the bath gas used in the sodium studies, is > 99% of the total gas mixture and methane, the bath gas used in the PBD studies is also >99% of the total gas mixture.

1.5 Determination of Equilibrium

For a general gas phase association reaction (Eq. 29), the ratio of product to reactant ion intensities is required to determine the equilibrium constant (Eq. 27 & 30). Ion intensities are recorded as a function of time using a Multi-Channel Scalar (MCS) card. The MCS card records ion counts as a function of time using the initial electron gun pulse as the trigger signal (i.e. $t=0$). Profiles are generated with 512 channels, using a dwell time of between 10-100 μ s per channel. This constitutes 1 electron gun pulse and therefore 1 scan.

The number of scans performed depends heavily on signal intensity and ion reactivity. The higher the signal intensity the lower the number of scans required. If the ion reactivity is low, equilibrium may be established later in the time-intensity profile. As ion intensity decreases with time, equilibria that are not established shortly after the ionization event require substantially more scans. The number of scans recorded varied from 500 to 25000.

Dwell time is the major factor in determining the length of the time-intensity profiles. Highly reactive ions are formed quickly, establish equilibrium quickly and decay quickly. For these ions short dwell times (10 -25 μ s) are required to extend the profile across all 512 channels, whereas, for ions of low reactivity and ions at low temperatures, the ion profiles need to be collected for a much longer time in order to capture the late forming equilibrium. To generate these profiles longer dwell times, or the time the MCS card spends collecting ion counts for one specific channel, need to be used. Figure 3 displays typical long living time-intensity profiles of a protonated monomer and PBD and Figure 4 displays the equivalent logarithmic plot.

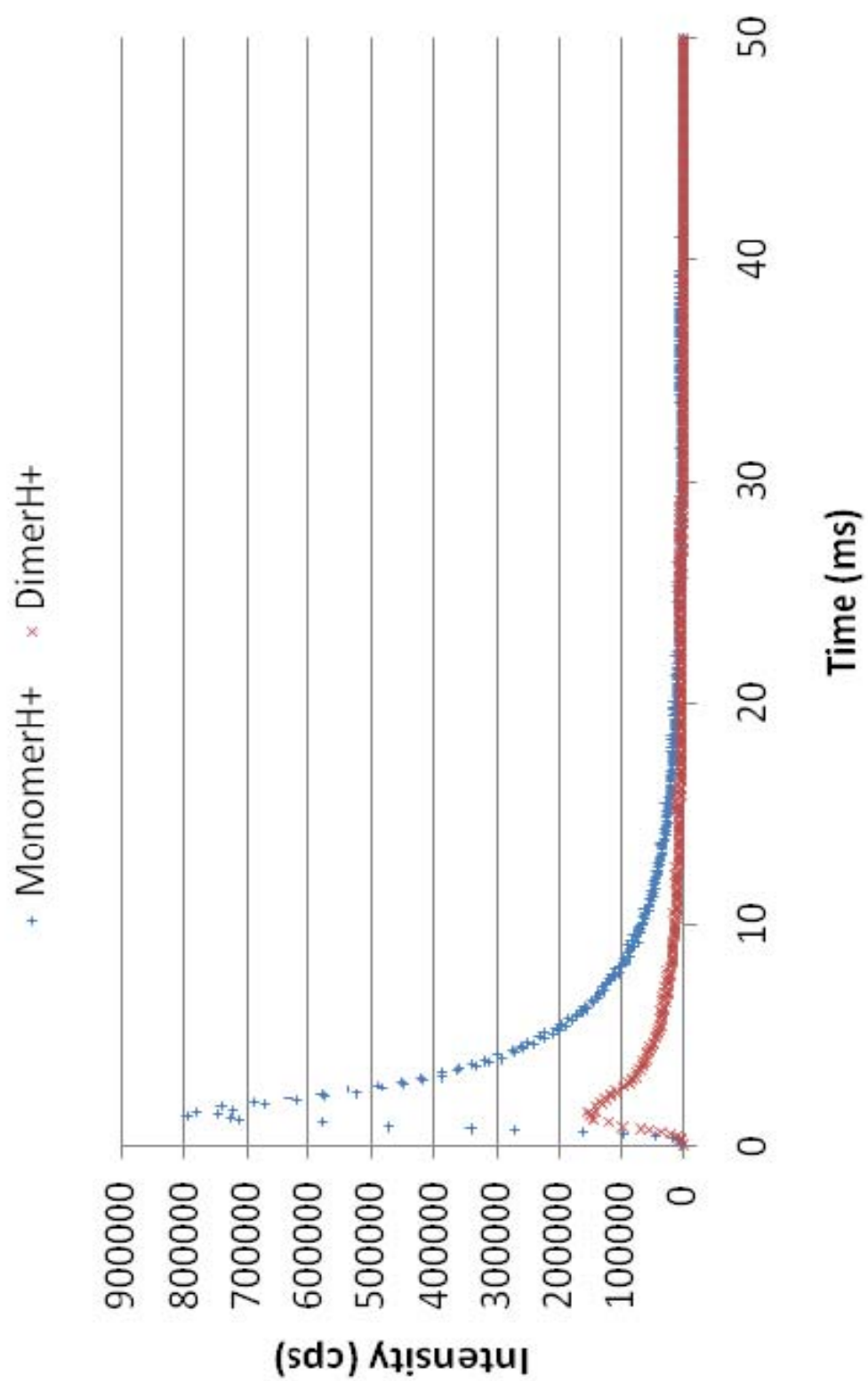


Figure 3 Time-Intensity Profile

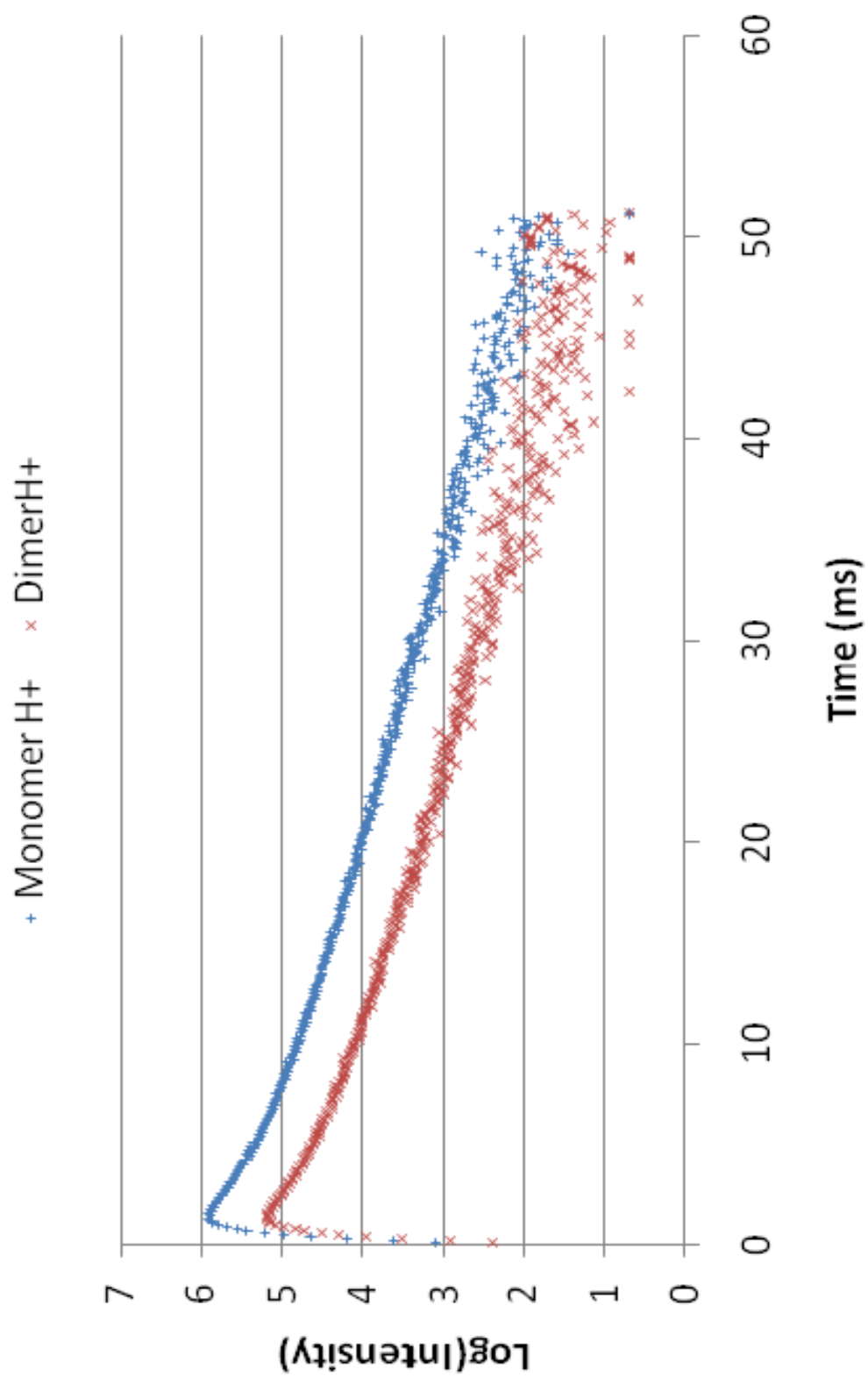


Figure 4 Logarithmic Time-Intensity Profile

The ion traces seen in Figures 3 and 4 are for protonated 1,1,1-trifluoro-2,4-pentanedione and the associated PBD. The temperature of the experiments was low ($< 100\text{ }^{\circ}\text{C}$) and as a result the ion intensity remains detectable for a long time period ($> 30\text{ ms}$).

In order to determine the equilibrium region for a gas phase association reaction, the ion intensities need to be normalized with respect to one another (Eq. 31 & 32).

$$n.i.(MonomerH^+) = \frac{I_{MonomerH^+}}{I_{MonomerH^+} + I_{DimerH^+}} \quad [31]$$

$$n.i.(DimerH^+) = \frac{I_{DimerH^+}}{I_{MonomerH^+} + I_{DimerH^+}} \quad [32]$$

The Normalized Intensity ($n.i.$) of both ions are then plotted. When the ion intensities of Figure 3 or 4 are normalized and plotted against time, Figure 5 is generated. Equilibrium is assumed to be established when the normalized intensity profiles of the two ions become horizontal to one another. The average ion intensity ratio, used in Eq. 27 and 30, is then obtained over the designated equilibrium region.

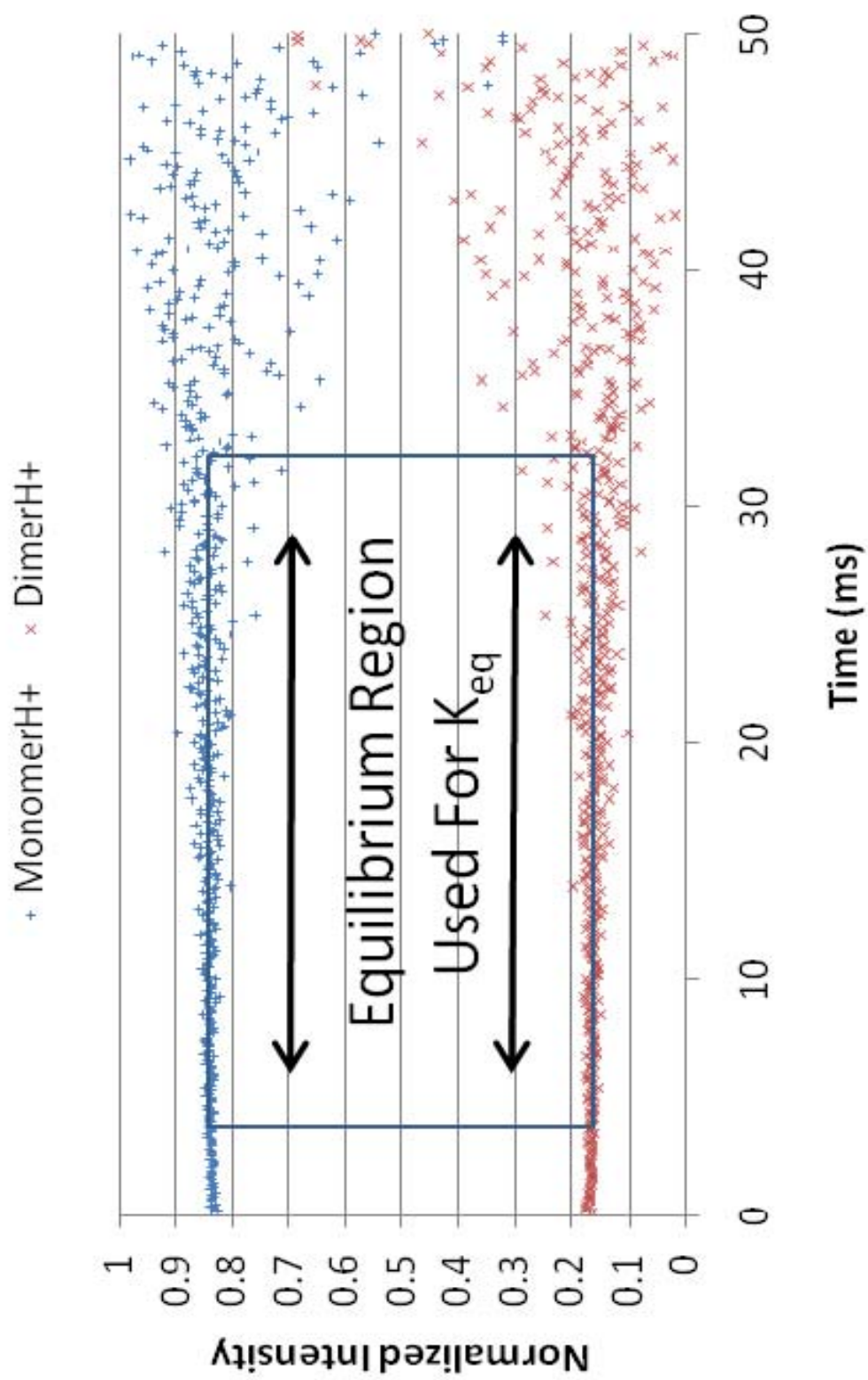


Figure 5 Normalized Time-Intensity Profile

The ion traces seen in Figure 5 establish equilibrium quite quickly (< 5 ms). The ion traces are able to be used in this case for approximately 30 ms or greater than 50 % of the entire profile length.

1.6 Computational Methods

A comparison of experimental and computational data has become standard practice in the interpretation of structures of species involved. Advances in computer hardware, software and computational theory have made high level electronic structure calculations practicable. The use of electronic structures calculations in validating proposed structures that may be formed in the gas phase is invaluable. The motive behind using computational techniques for this thesis was to predict structures involved in the association reactions explored and compare the experimentally determined values against the calculated enthalpy and entropy changes to gain insight into the structure and bonding of the ion-molecule complexes.

The choice of basis set and level of theory is dependent on a number of factors. Often the size of the system being studied is the first step in determining the method to be used. Systems containing hundreds to thousands of atoms require much more computational resources than systems containing a few atoms. Large systems may employ molecular mechanics methods. Molecular mechanic simulations use the laws of classical physics to predict the structures and properties of molecules.¹⁵ These simulations are much less computationally demanding.

In contrast, electronic structure calculations can be performed on smaller systems. Electronic structure methods use the laws of quantum mechanics as the basis for their computations.¹⁵ Electronic structure methods can be broken down into two types: *ab initio* and semi-empirical methods. Semi-empirical methods employ parameters derived from experimental data to simplify the computation. *Ab initio* methods use no experimental parameters in their

computations and rely on the values of a small number of physical constants. The *ab initio* methods approximate the Schrodinger equation using a series of rigorous mathematical approximations.¹⁵ The simplest *ab initio* method, the Hartree-Fock (HF) Self Consistent Field (SCF) Theory, assumes that each electron experiences an average field from the other electrons. The HF method ignores the instantaneous repulsion between electrons (electron correlation). Møller-Plesset (MP) theory is an *ab initio* method that takes electron correlation into account.¹⁶

Density Functional Theory (DFT) is used as an alternative to *ab initio* calculations for larger molecules.¹⁷ DFT is derived from quantum mechanics and includes limited electron correlation. DFT is attractive because of its lesser computational demand and its ability to yield results that are comparable with experiment and more resource demanding computational techniques.^{18,19} The B3LYP method is an example of a DFT method which has been used in this study. In this study a number of *ab initio* and DFT theories were used depending on the system being studied and the computational resources available at the time.

The basis set is a mathematical representation of molecular orbitals that limit each electron to a specific region of space. Standard basis sets apply linear combinations of Gaussian functions to describe each orbital. Split valence basis sets (3-21G, 6-311G etc.) have two or more sizes of basis functions for each valence orbital. A triple split valence set, 6-311G, uses 6 Gaussian functions to describe the core shell orbital and 3 basis sets to describe the valence shell. The valence basis sets consist of 3, 1 and 1 Gaussian functions respectively.^{20,21} During most molecular bonding it is the valence electrons that take part in the bonding and thus require a more accurate description of the valence orbitals. A triple split valence basis set uses one of three possible sizes to describe the valence orbital on each atom. The different sizes of orbitals are used to account for changes in the molecular environment.

Polarization and diffuse functions can be included in the basis set to give a more accurate

description of molecular orbitals. Atomic orbitals are polarized or distorted from their idealized atomic shapes to provide optimal bonding in molecules. Polarization functions are often useful when calculations are compared against molecular systems involving excited states. Polarization functions add orbitals with higher angular momentum than that required for a ground-state description of the atom.²² As an example, the 6-311G(d,p) (or 6-311G**) basis set includes two polarization functions. The first polarization function is the addition of d-type orbitals to heavy atoms (non-hydrogen). The second polarization function is the addition of p-type orbitals to hydrogen atoms. The polarization function on the hydrogen atom generally allows for a more accurate representation of hydrogen bonding as the addition of p-type orbitals to hydrogen mimic the molecular environment better.

Diffuse functions can also be included in the basis sets. Diffuse functions are added basis functions that are more spread out and allow for the orbitals to occupy a larger region of space.²³ Diffuse functions are particularly useful when electrons are relatively far away from the nuclei as in the case of anion containing systems and systems with relatively long bonds. A similar convention is used to include diffuse functions in a basis set. For example, a 6-311++G** basis set adds diffuse s- and p-type orbitals to the first and second row atoms (Li –Cl) (the first +) and a set of diffuse s-type functions to hydrogen atoms (the second +).

Another type of computational method that is employed in this study is the compound method. Compound methods perform a series of calculations using a single keyword. G3(MP2) is an example of a compound method. G3(MP2) is useful as it applies a very high level of theory while minimizing the computational demand. G3(MP2) accomplishes this by successively increasing the level of theory and electronic energy calculation. G3(MP2) first performs a geometry optimization and frequency calculation at the HF/6-31G(d) level of theory. The system is then reoptimized at the MP2(Full)/6-31G(d) level of theory. This is the geometry that is used

for the electronic single point calculations. The final single point calculation is a MP2/G3(MP2)large calculation.^{24,25}

The computations performed in this study used the HF, B3LYP and MP theories employing a number of basis sets. The B3LYP/6-31+G(d,p) basis set has been shown to be satisfactory for the geometry optimization of hydrogen bonded species, however, the basis set is not sufficient to describe the electronic dispersion effects.²⁶ A method that is used regularly combines the DFT geometry and frequency calculation with an *ab initio* MP electronic structure calculation. This hybrid method is computationally advantageous and agrees well with experimental data.

All calculations were performed using the Gaussian 03 program.²⁷ The results were viewed and the molecular images were created using the Gaussview 3.0 program.²⁸ The calculations were performed on the Shared Hierarchical Academic Research Computing Network (SHARCNET). The facilities at SHARCNET allow for four 2.20 GHz Opteron processors using 4 GB of shared memory to perform the computations.

2.0 Sample Preparation – Sodium

One objective of this project was to obtain sodium vapour inside of the ion source in sufficient amounts at the lowest temperature possible. Previous methods of sodium ion production in HPMS experiments had been limited to temperatures $> 285\text{ }^{\circ}\text{C}$.²⁹ To this end various sodium-containing substances were investigated as viable sources of sodium vapour. Side-products of the vaporization process as well as melting temperature's were considered as the main deciding characteristics while investigating different sodium-containing solids. Sodium metal (m.p. $97\text{ }^{\circ}\text{C}$) was chosen due to the advantageous melting point and relatively low amount of side products upon volatilization. Other materials that were attempted with some to no success, respectively, were sodium valerate (m.p. $140\text{ }^{\circ}\text{C}$), sodium nitrate (m.p. $290\text{ }^{\circ}\text{C}$) and sodium dodecasulphate (m.p. $206\text{ }^{\circ}\text{C}$).

Bare sodium, being an alkali metal, is highly reactive. Sodium reacts with water vapour and oxygen that are present in the air when exposed to it. The reaction turns the metallic-silver gloss of pure sodium to a gray-white flat appearance within a very short time period (1-2 minutes) upon exposure to the laboratory atmosphere. The discoloration of the sodium surface is essentially oxide formation. The white colour comes from the production of disodium oxide (Na_2O) as the primary product of the reaction between sodium and air.³⁰ The oxide formation is unwanted as it has an extremely high melting point ($>1100\text{ }^{\circ}\text{C}$) and it also could introduce elemental oxygen into the high-pressure reaction chamber. The oxide formation was minimized by purchasing sodium metal covered in kerosene and limiting the exposure time of the metal to the atmosphere. Sodium was shipped and stored in a glass container under kerosene, prior to introduction to the ion source, to prevent oxidation.

2.1 Sodium Sample Container

Once sodium metal had been selected as the source for sodium vapour inside the ion source, optimal conditions needed to be determined. The conditions desired were those to produce the longest lifetime and the lowest temperatures possible for a useable sodium ion signal. The normal melting point of sodium metal is 97 °C. The solid sample must be heated in close proximity to the ion source. If the sample was not heated inside the ion source, but further down the gas transfer line, the number density of sodium atoms in the source could be severely affected. If any point along the gas transfer line was not heated properly (i.e. a cold spot), condensation of the sodium vapour would occur, thereby lowering the sodium concentration.

The location of the solid sample was thus restricted to inside the ion source block. This was done to avoid re-condensation of the sodium metal along the transfer line from the heated reservoir to the block and therefore ensure the maximum partial pressure of sodium gas. Since it was required that the sodium sample be placed inside of the ion source block each time the sodium sample was depleted, the HPMS system needed to be shut down and brought to atmosphere in order to replenish the sodium metal. The procedure required replacement of the exhausted sodium source and restoration of a working vacuum pressure inside the spectrometer which was time intensive (ca. 16 hours). Due to the long delay and possible complications associated with dismantling the mass spectrometer and ion source, the longest lifetime of sodium ion intensity was desired to minimize these downtimes.

The solid sample needed to be placed inside the ion source block and then the source block needed to be manoeuvred back into the Allaria chamber of the spectrometer. This required the solid sample to be immobilized inside the source to ensure a reliable and consistent location, a precursor to a reliable and consistent ion signal.

2.2 *The Top Hat*

The first attempt at immobilizing the metallic sodium produced unsatisfactory results. The sodium ion and cluster ion signals generated using the top hat (Figure 6) were inconsistent and short-lived. Ion signals were measured at very low intensities and were unusable after a few hours in the presence of a clustering gas.



Figure 6 Stainless Steel Top Hat

The top hat was a non-magnetic stainless steel cup fabricated by the University of Waterloo Machine Shop. It was designed to fit into a pre-existing unused port on the source block. Figure 7 shows the position of the top hat relative to the rest of the source block and electron entrance aperture.

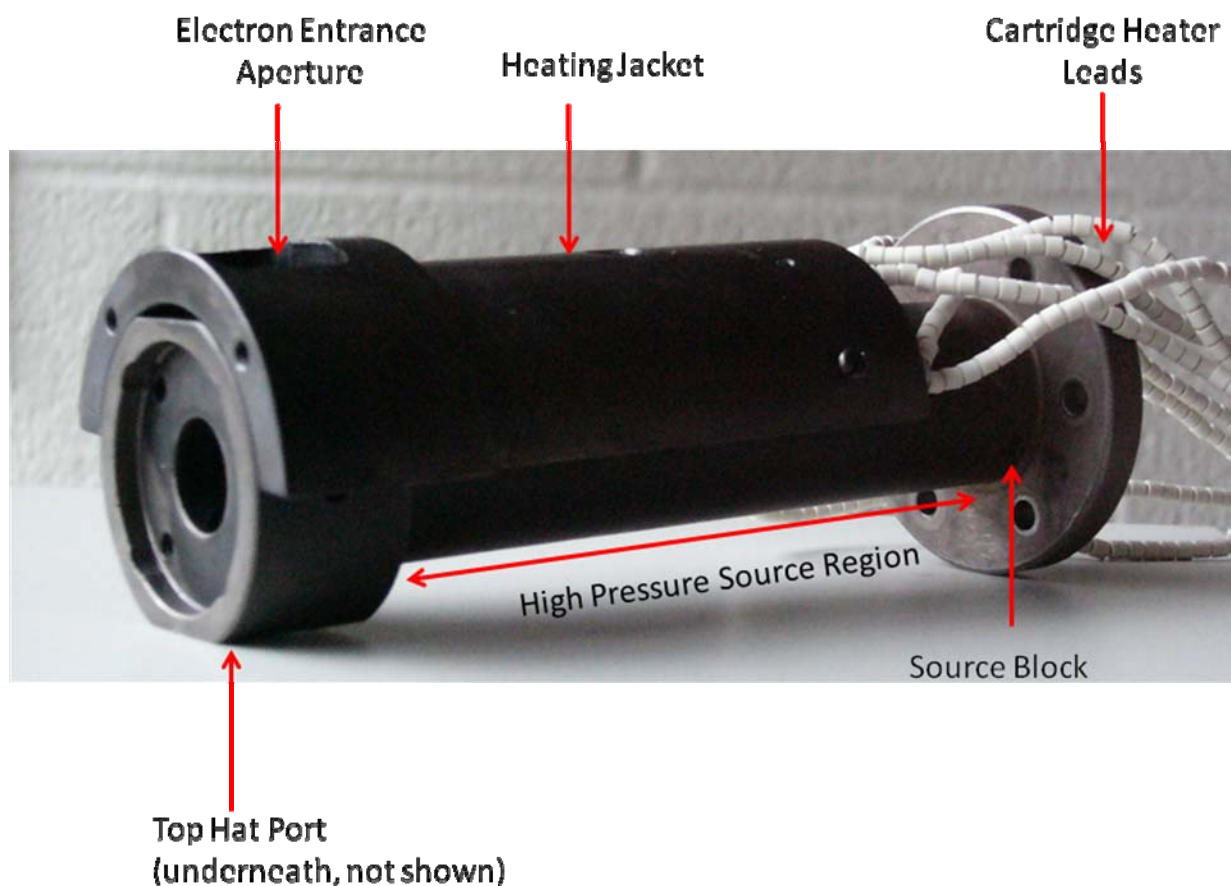
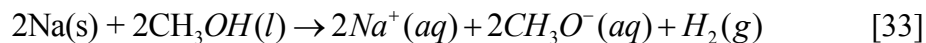


Figure 7 Ion Source with Heating Jacket

The position of the top hat was directly beneath the electron entrance aperture. The electron bombardment of the clustering gas seemed to passivate the limited surface area of the sodium metal. Using the top hat, it was possible to pack a large amount of the malleable sodium into the cup but with only a top layer exposed to the environment inside the ion source. Upon removal of the sample cup, the top layer was discoloured with a hard black surface. Transferring the contents of the cup to a beaker of methanol, a vigorous reaction occurred liberating hydrogen gas, indicating the presence of sodium (Eq. 33).



Increasing the temperature inside the source ($> 350\text{ }^{\circ}\text{C}$) did not produce a sodium ion signal but the reaction of sodium with methanol could be observed once the top hat was removed from source block. If a sodium oxide layer, or sodium containing solid layer was formed on the top of the sodium metal, the vapour pressure of sodium would be affected drastically. The vapour pressure of sodium would be greatly reduced due to the high melting point of sodium oxides and sodium containing solids, which effectively encapsulate the pure sodium metal.

The top hat was placed directly underneath the electron entrance aperture and the surface of the sodium metal seemed to be inactivated by the harsh environment produced by the ionization process. The placement of the sodium and the relative low surface area to volume ratio were addressed with the next attempt at an immobilized sodium container.

2.3 *The Glass Ampoule*

The term glass ampoule is somewhat of a misnomer but can be used to describe the next sample holder. Ampoules are commonly known as phials (vials) which are glass bottles used for medicines. Often ampoules are hermetically sealed. This is not the way in which the term is referred to in this project. Figure 8 shows a typical vessel that is referred to as a glass ampoule. The glass ampoule is made in-house starting with a glass pipette. The capillary end of the ampoule is left open to allow for both, the insertion of the solid sodium sample at atmospheric conditions and the release of sodium vapour to the ion source inside the spectrometer. The other end of the glass ampoule is melted using a propane torch. This effectively seals one end of the glass ampoule, leaving one end open for insertion and removal of the sodium metal.

Sodium metal was dried and rolled into long thin cylinders to increase the surface area and to permit the insertion of the sodium into the ampoule. The ampoule was then fashioned with a wire cage to immobilize it inside the ion source (see Figures 8 and 9).

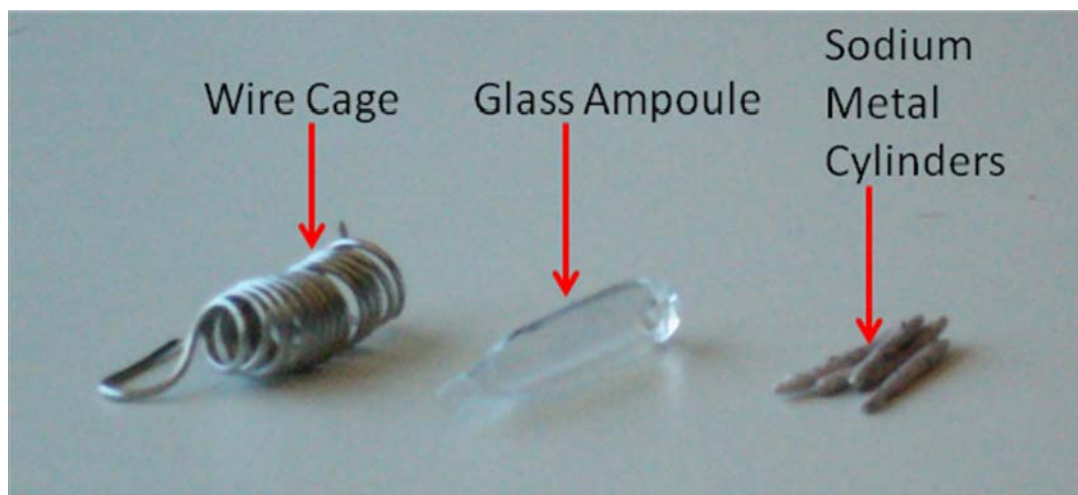


Figure 8 Glass Ampoule with cage and Sodium Separate



Figure 9 Glass Ampoule in Cage (sodium not visible)

The cage had two main functions; to hold the ampoule in a fixed position inside the ion source and to hold the ampoule tight against the wall of the ion source block. It was necessary for the ampoule to be in firm contact with the inside surface of the source block such that the thermal energy supplied by the heaters, which are in direct contact with the outside surface of the ion source block (Figure 7), was efficiently transferred to the sodium metal sample. This intimate

contact was necessary to generate sodium ion signals in the low temperature region (140 °C) and to maximize the lifetime of the sodium ion signal.

Using the glass ampoule signal consistency was an issue. The duration of sodium ion intensity varied greatly between experiments. The lifetime ranged from 2-10 days. Ion intensity was low and thus equilibrium measurements over a small temperature range proved difficult. Upon removal of the glass ampoule it was apparent that reactions occurred between the glass walls and the sodium metal. Significant discolouration and deformations were present in the glass ampoule.

Upon removal of the glass ampoule it was often noticed that a considerable amount of the sodium metal had not been vapourized. Despite quite high temperatures (350-400 °C) no sodium ion signal could be detected, however, upon removing the ampoule and placing the entire contents in a bath of methanol, hydrogen gas was liberated. As in the case of the top hat sodium container, the surface of the sodium metal seemed to be passivated, inhibiting sodium vapour production.

Two major insights were gained from these experiments with the glass ampoule; first, the glass was not inert enough to prevent reaction with the sodium metal and secondly, not enough thermal energy was supplied to the sodium metal to vapourize it. This led to the third and current design of the sodium sample holder.

2.4 *The Stainless Steel Boat*

The stainless steel boat was constructed to provide an inert container for the sodium metal and to ensure a uniform distribution of thermal energy to the container and subsequently the sodium metal contained within. The boat was designed to maximize the surface contact between the container and the walls of the source. A non-magnetic stainless steel container was produced by the University of Waterloo Machine Shop (Figure 10).

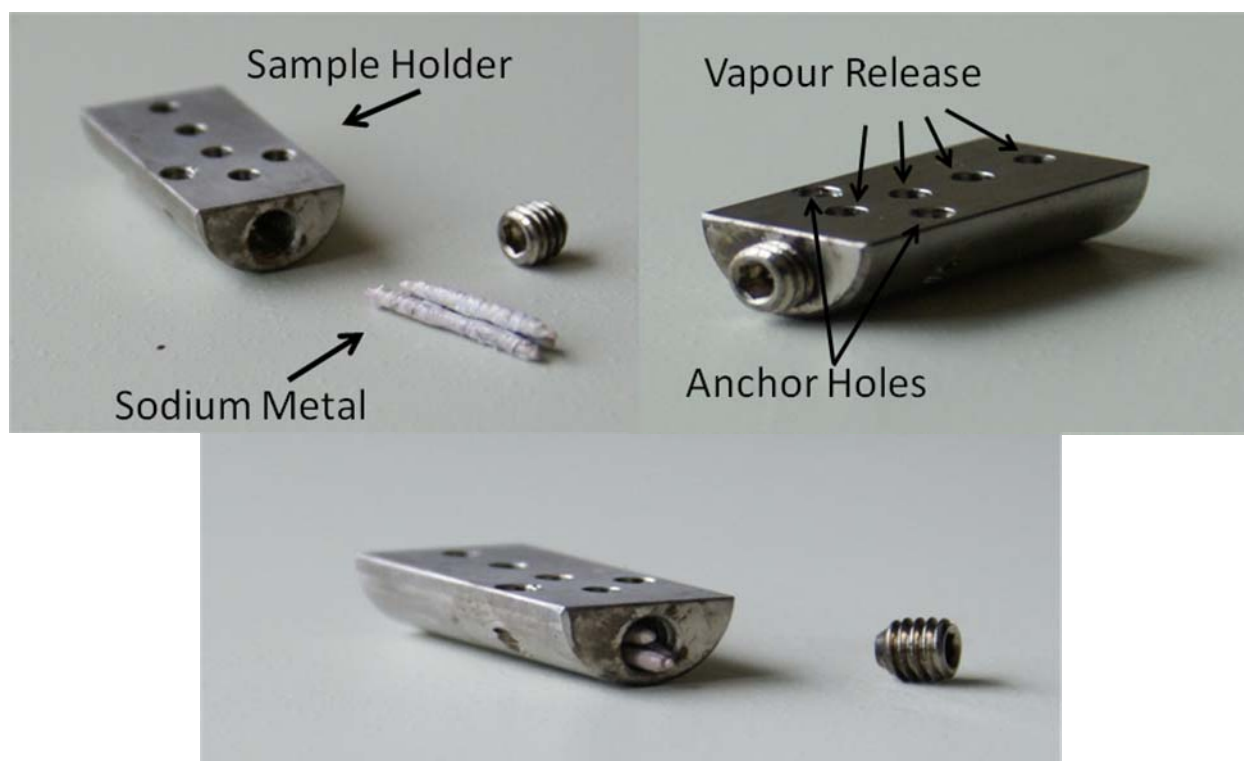


Figure 10 **The Stainless Steel Boat**

The outer diameter of the boat matched the inner diameter of the source block. The boat thus occupied one half of the diameter of the source block. The boat contained a bore through the middle, with a screw cap on one end, to allow for cylinders of sodium to be placed inside. The screw cap prevented liquid sodium from flowing out of the container. On the flat (top) surface of the boat, six holes were machined. Four of the holes penetrated the inner bore allowing for vapour release of the sample. The other two holes were machined on the extremities of the boat, not penetrating the inner bore, to allow for a clip to immobilize the boat inside the ion source block. A carefully constructed spring clip was attached to the two outer holes to act as an immobilizing agent for the container inside the source. The clip and boat were then inserted inside the ion source in close proximity to the electron entrance aperture.

The boat provided a consistent and reproducible sodium ion signal for an extended period of time at relatively low temperatures. Equilibrium measurements were possible at 140 °C. The average lifetime of the sodium ion signal was 2 weeks depending on the temperature range being studied. Upon removal of the boat from the source very little to no sodium remained. Also, the stainless steel boat did not seem to react whatsoever with the sodium and very little discolouration could be noticed on the stainless steel boat.

The stainless steel boat was the container used for the sodium experimental data presented in this thesis.

3.0 Proton Bound Dimers

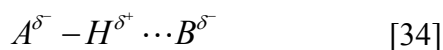
3.1 Introduction to Proton Bound Dimer Systems

Molecular interactions in the chemical, biochemical and biological world are all governed, at least in some part, by hydrogen bonding. Arguably, hydrogen bonding is one of the most important interactions governing the structure and behaviour of molecules. The extensive network of hydrogen bonding is responsible for the high melting point and high boiling point of H₂O. The effects are quite dramatic when comparing species capable of hydrogen bonding against those which cannot. For example, the boiling points of water, dimethylether and oxygen difluoride vividly exemplify the importance of hydrogen bonding (see Table 2).³¹ A solid understanding of hydrogen bonding is fundamental and invaluable to all types of chemists.

Table 2 Boiling Points Summary of Simple Oxygen Containing Species

Species	Boiling Point (°C)
(CH ₃) ₂ O	-138
F ₂ O	-224
H ₂ O	+100

Hydrogen bonding is ubiquitous and one of the principal intermolecular forces.⁹ Hydrogen bonding involves a hydrogen atom and an electronegative atom, usually oxygen, fluorine or nitrogen. Hydrogen bonds are attractive interactions occurring between hydrogen atoms and the electronegative atoms as shown in Eq. 34, where A and B contain an electronegative atom.



The hydrogen atom illustrated in Eq. 34 is left with a partial positive charge due to the electron density being polarized by the electronegative elements. Due to the relatively small size

of the hydrogen atom, the resulting partial positive charge represents a region of large charge density, making it an excellent electron acceptor.³²

Hydrogen bonding can be classified into three main categories; intermolecular, intramolecular and ionic. Intermolecular hydrogen bonds are formed between molecules. Figure 11 displays a very simple but important intermolecular hydrogen bond between water molecules.

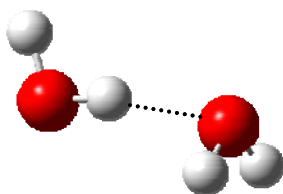


Figure 11 **Intermolecular Hydrogen Bond**

The hydrogen bond between two neutral water molecules has a bond energy between 10 and 20 kJ mol⁻¹.¹

Similarly, hydrogen bonds can also be formed between electronegative atoms contained within the same molecule which is referred to as an intramolecular hydrogen bond. A simple example to demonstrate this is the molecule 1,3-propanediol (Figure 12).

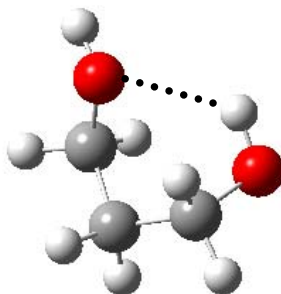


Figure 12 **Intramolecular Hydrogen bond**

The third and final class of hydrogen bonding is the ionic hydrogen bond (IHB). The IHB is a unique form of hydrogen bonding. The IHB is of considerable interest to gas phase chemists as ion formation is a prerequisite for mass spectrometry. The IHB is pervasive in nearly all HPMS experiments. Unique to the IHB is the magnitude of the binding energy. IHBs are routinely found to have bond strengths up to $\approx 150 \text{ kJ mol}^{-1}$ or one third the strength of a typical covalent bond. The binding energy of the strongest IHB known has been measured at 192 kJ mol^{-1} for the HF_2^- anionic complex.³³ For a typical IHB, water is revisited. The protonated water dimer (Figure 13) forms an IHB with a binding energy of 135 kJ mol^{-1} .⁴

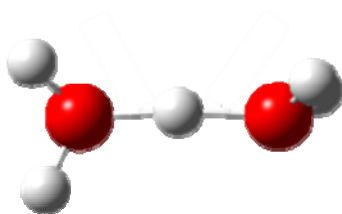


Figure 13 **Ionic Hydrogen Bond**

The chemical implications of IHBs are vast. The strong interactions of IHBs are of paramount importance in ionic clusters, electrolytic solutions, nucleation and acid base chemistry along with many bioenergetic processes.³⁴ By studying ionic species in the gas phase, solvent effects are nonexistent and the intrinsic properties of an IHB can be explored and quantified.

One aspect of this thesis investigated gas phase association reactions involving ketone and β -diketone species. Protonated ketone and diketone ions readily associate and form IHBs. By quantitatively studying these clustering reactions in the gas phase, insight into the relationship between hydrogen bonding and molecular structure is gained. The chemistry of mono keto monomers is relatively straightforward. Simple ketones exist largely in the keto form before ionization.³⁵ The negligible amount of tautomerization in the simple mono ketones simplifies the range of isomers explored by electronic structure calculations. Conversely, the chemistry of

diketone species is not as straightforward. The formation of a stabilizing intramolecular hydrogen bond arises when considering diketones.³⁶ This stabilizing intramolecular hydrogen bond in diketone species arises in the enol tautomer. It is well known that the enol form of β diketones is characterized by a strong intramolecular hydrogen bond.³⁷⁻⁴⁰ The keto-enol tautomerization of a few diketone species is examined in this thesis.

Keto-enol tautomerization is one of the most important subjects in the chemistry of organic ketones and their corresponding ions.⁴¹ Diketone species constitute an important class of molecules prone to this tautomerism and intramolecular hydrogen bond formation. In solution, the keto to enol tautomerism is known to be a facile bimolecular or higher order process.⁴² The gas phase isomerisation reaction is not as facile. In the gas phase, the unimolecular isomerization of a ketone to its enolic counterpart, which is generally more stable⁴³, is difficult.⁴⁴ The difficulty arises from a high-energy barrier separating the ketone from its generally more stable enolic isomer.⁴⁵ The energy barrier is lowered considerably if the isomerization is catalyzed, which has been shown for ionized acetaldehyde.⁴⁶ The specific keto-enol tautomerization reactions studied in this paper will be discussed below.

Another aspect of this thesis is to investigate the effects of fluorination in 2,4-pentanedione. The effects of fluorine substituents on the stability and reactivity of ionic species has been of interest to physical organic chemists since the beginning of gas phase ion chemistry.^{47,48} Fluorine and trifluoromethyl substituents have been demonstrated to be capable of dramatically altering the stabilities of ionic species in both gas and solution phases.⁴⁹ By studying tri- and hexa- fluorinated 2,4-pentanedione in the gas phase, the intrinsic effects of the fluorination can be deduced. There has been a moderate amount of information published on the effect of fluorinating acetone.⁵⁰⁻⁵² The results show a linear decrease in the proton affinity during the stepwise substitution of fluorine atoms when comparing acetone through to hexafluoro-

acetone. The linear decrease in proton affinities is attributed to inductive effects due to the presence of the fluorine substituents and intramolecular hydrogen bond formation.⁵¹ Similar trends are expected for the β -diketones, 2,4-pentanedione and their tri- and hexa-fluorinated derivatives. The inductive effects of electron withdrawing substituents are known to increase the enol content of β -diketones.⁵³⁻⁵⁷ The presence of fluorine atoms in β -diketones has a dramatic effect. The enol form of the diketone species is favoured but as the the number of fluorine atoms is increased, the strength of the intramolecular hydrogen bond is decreased.⁵⁸ Due to the expected decrease in proton affinity, the tri- and hexa- fluorinated derivatives might be expected to have weaker binding energies upon PBD formation.

3.2 *Butanone*

The association reaction involving butanone and protonated butanone is given in Eq. 35.



The reaction was observed over a temperature range of 193 to 287 °C. Depending on the temperature, between 1 and 25 μL was injected into a heated 5 L stainless steel reservoir. The bath gas for the generation of the butanone van't Hoff plot was methane, which comprised more than 99% of the total gas mixture.

For a typical experiment the butanone is injected into the reservoir and allowed to equilibrate for thirty minutes before the gas mixture is flowed into the ion source. The electronics are then turned on and allowed to equilibrate to allow for any electronic drift effects. Time

intensity profiles were collected for mass-to-charge (m/z) 73 and 145 corresponding to the protonated butanone monomer and dimer, respectively. A van't Hoff plot was generated over $\approx 100^\circ$ temperature range (Figure 14). Using Eq. 17 and 18 the enthalpy and entropy values of the association reaction were obtained. The enthalpy change was determined to be $-134 \pm 2.5 \text{ kJ mol}^{-1}$ and the entropy change was determined to be $-145 \pm 10 \text{ J mol}^{-1} \text{ K}^{-1}$.

Ab initio and DFT calculations were performed using a number of different methods. The calculation that agreed best with the experimental values used the B3LYP/6-311++G(3df,3pd) basis set for the geometry optimization, followed by a MP2/6-311++G(3df,3pd) single point calculation. The calculated ΔH_{rxn} and ΔS_{rxn} values for the formation of the butanone PBD are -135 kJ mol^{-1} and $-150 \text{ J mol}^{-1} \text{ K}^{-1}$, respectively. Similar results were obtained using different optimization methods and levels of theory. The results for the butanone experiments and theory are tabulated in Table 3.

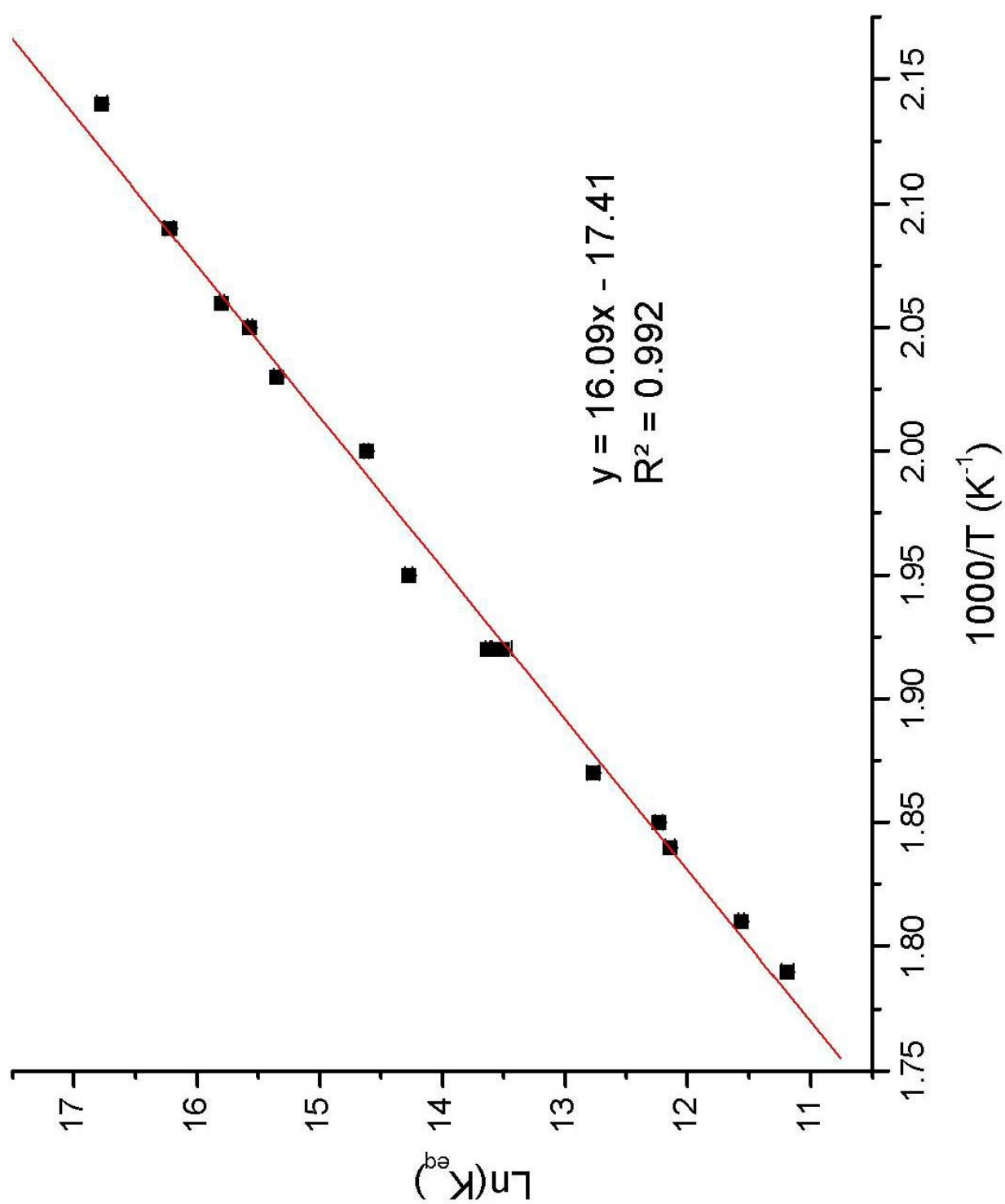


Figure 14 van't Hoff Plot of Butanone

Table 3 Butanone Thermochemical Data, Experimental and Calculated Summary

Source	ΔH (kJ mol ⁻¹) (kcal mol ⁻¹)	ΔS (J mol ⁻¹ K ⁻¹) (cal mol K ⁻¹)	ΔG (kJ mol ⁻¹) (kcal mol ⁻¹)
Current HPMS Experiment	-133.8 (-32.0)	-144.8 (-34.6)	-90.6 (-21.7)
Previous HPMS Experiment ⁵⁹	-128.0 (-30.6)	-133.1 (-31.8)	-88.4 (-21.1)
Previous ICR Experiment ⁶⁰	-131.0 (-31.3)	-129.0 (-30.8)	-92.6 (-22.1)
MP2/6-311++G(3df,3pd)// B3LYP/6-311++G(3df,3pd)	-134.6 (-32.2)	-149.8 (-35.8)	-89.9 (-21.5)
MP2(FULL)/6-311+G(d,p)// MP2(FULL)/6-31G(d)	-131.1 (-31.3)	-137.69 (-32.9)	-90.0 (-21.5)
B3LYP/6-311++G(3df,3pd)	-125.6 (-30.0)	-149.8 (-35.8)	-80.9 (-19.3)
G3(MP2)	-123.3 (-29.5)	-138.8 (-33.2)	-81.9 (-19.58)

The agreement between theory and experiment in the case of butanone is very good. The binding energy of the IHB formed in the PBD of butanone is 134 kJ mol^{-1} . This is in excellent agreement with predicted binding energy (135 kJ mol^{-1}) for the reaction presented in Figure 15.

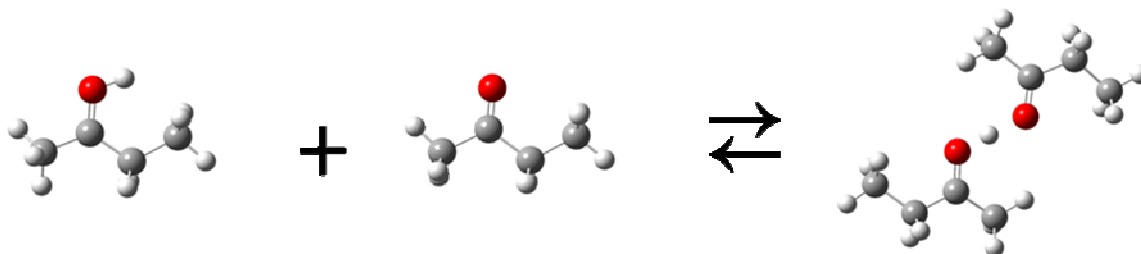


Figure 15 The MP2/6-311++G(3df,3pd)// B3LYP/6-311++G(3df,3pd) Optimized Representation of the Butanone PBD Formation

The butanone association reaction (Eq. 35) has been studied previously.^{59,60} The agreement between experimental values of the binding energy of the PBD of butanone is also good. The binding energy value of 135 kJ mol^{-1} (reported here) is slightly higher than previous experiments which reported values of 128^{59} and $131^{60} \text{ kJ mol}^{-1}$. The excellent agreement between previous experiments and current theory suggest that the structure of the PBD of butanone is accurately depicted in Figure 15 which contains one IHB with a binding energy of $134 \pm 2.5 \text{ kJ mol}^{-1}$.

The experimentally obtained entropy values are also in very good agreement with the calculated values. The experimentally determined entropy change is $-145 \pm 10 \text{ J mol}^{-1} \text{ K}^{-1}$ which is in very good agreement with the calculated value of $-150 \text{ J mol}^{-1} \text{ K}^{-1}$. The entropy values are also in good agreement with the previous experiments which reported entropy values of $-133 \text{ J mol}^{-1} \text{ K}^{-1}$ and $-129 \text{ J mol}^{-1} \text{ K}^{-1}$.^{59,60}

The agreement for the change in Gibbs free energy of association is very good between the current experiment and the best theoretical calculations performed to date. The experimental ΔG_{298} is $-90.6 \pm 8 \text{ kJ mol}^{-1}$, which correlates well with the calculated ΔG_{298} of $-89.9 \text{ kJ mol}^{-1}$.

The calculated arrangement of the PBD of butanone shown in Figure 15 accurately describes the bonding seen experimentally. The excellent agreement with current theory and previous results suggest an accurate measurement of the binding energy of the IHB in the PBD of butanone.

3.3 2-Pentanone

The association reaction involving 2-pentanone and protonated 2-pentanone is given in Eq. 36.



The reaction was observed over a temperature range of 141 to 253 °C. Depending on the temperature, between 1 and 25 µL was injected into a heated 5 L stainless steel reservoir. The bath gas for the generation of the 2-pentanone van't Hoff plot was methane, which comprised more than 99% of the total gas mixture.

For a typical experiment, the 2-pentanone liquid is injected into the reservoir and allowed to equilibrate for thirty minutes before the gas mixture is introduced into the ion source. The electronics are then turned on and allowed to equilibrate (\approx 15 minutes) to allow for any electronic drift effects. Time-intensity profiles were collected for m/z 87 and 173 corresponding to the protonated 2-pentanone monomer and dimer, respectively. A van't Hoff plot was generated over \approx 110 ° temperature range (Figure 16). Using Eq. 17 and 18, the enthalpy and

entropy values of the association reaction were obtained. The enthalpy change was determined to be $-126 \pm 2.5 \text{ kJ mol}^{-1}$ and the entropy change was determined to be $-144 \pm 10 \text{ J mol}^{-1} \text{ K}^{-1}$.

Electronic structure calculations were performed using a number of different methods. The calculation that agreed best with the experimental values uses the G3(MP2) method. The calculated ΔH_{rxn} and ΔS_{rxn} are -129 kJ mol^{-1} and $-140 \text{ J mol}^{-1} \text{ K}^{-1}$, respectively. Similar results were obtained using different optimization methods and levels of theory. The results for the 2-pentanone experiments and theory are tabulated in Table 4.

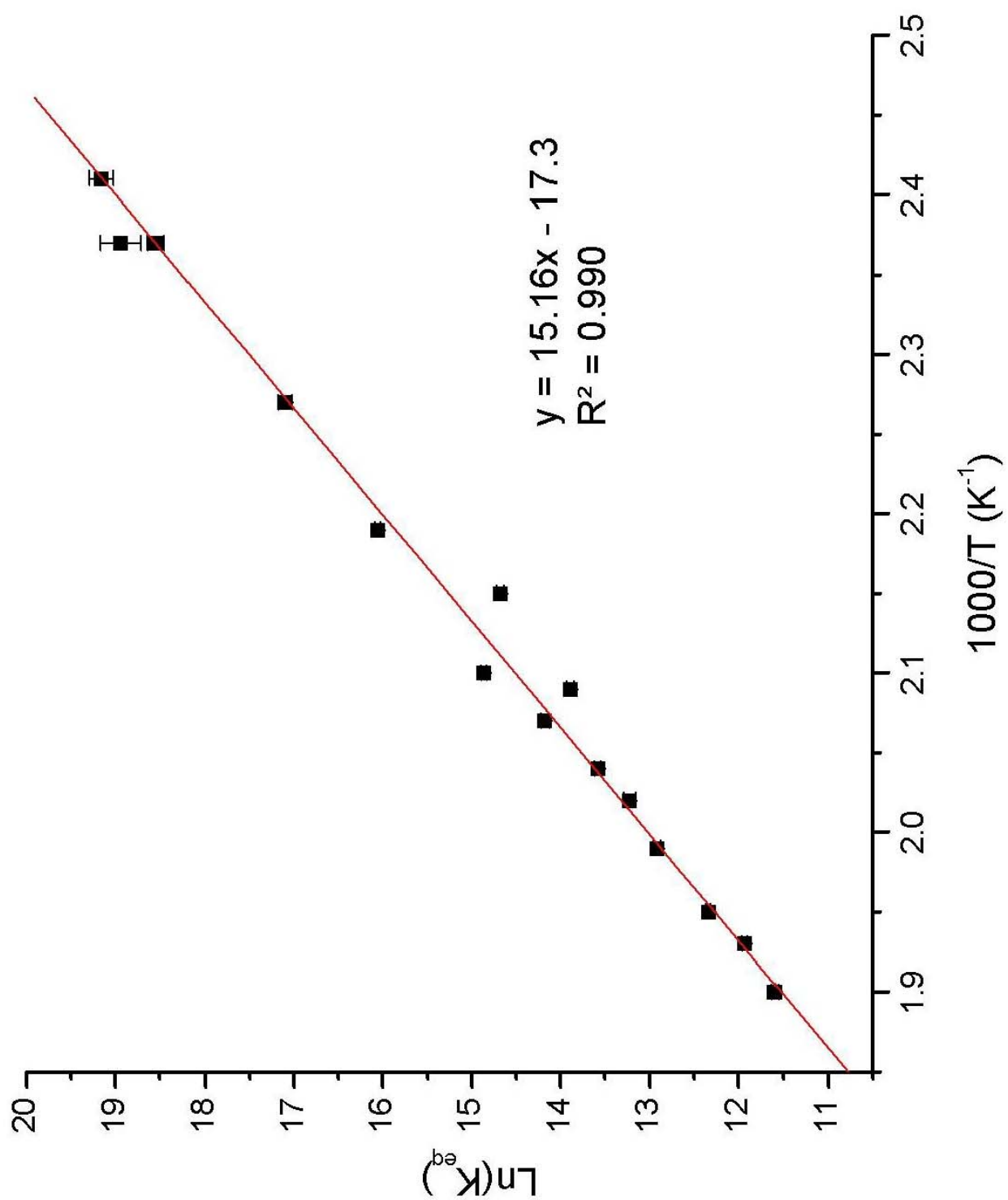


Figure 16 van't Hoff Plot of 2-Pentanone

Table 4 2-Pentanone Thermochemical Data, Experimental and Calculated Summary

Source	ΔH (kJ mol ⁻¹) (kcal mol ⁻¹)	ΔS (J mol ⁻¹ K ⁻¹) (cal mol K ⁻¹)	ΔG (kJ mol ⁻¹) (kcal mol ⁻¹)
Current HPMS Experiment	-126.1 (-30.1)	-144.2 (-34.5)	-83.1 (-19.9)
Previous HPMS Experiment ⁵⁹	-125.5 (-30.0)	-128.0 (-30.6)	-87.3 (-20.9)
G3(MP2)	-128.6 (-30.7)	-140.0 (-33.5)	-86.9 (-20.8)
MP2(FULL)/6-311+G(d,p)// MP2(FULL)/6-31G(d)	-129.7 (-31.0)	-141.9 (-33.9)	-87.4 (-20.9)
B3LYP/6-31+G**	-130.3 (-31.1)	-140.0 (-33.5)	-88.6 (-21.2)
MP2/6-311+G**// B3LYP/6-31+G**	-131.8 (-31.5)	-140.0 (-33.5)	-90.1 (-21.5)

The agreement between theory and experiment in the case of 2-pentanone is very good. The binding energy of the IHB formed in the PBD of 2-pentanone is 126 kJ mol^{-1} . This is in good agreement with predicted binding energy (129 kJ mol^{-1}) for the reaction presented in Figure 17.

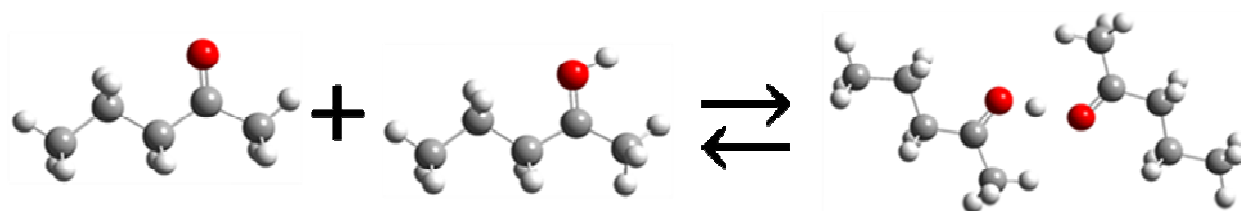


Figure 17 The G3(MP2) Optimized Representation of the 2-Pentanone PBD Formation

The 2-pentanone association reaction (Eq. 36) has been studied previously.⁵⁹ The agreement between experimental values of the binding energy of the PBD of 2-pentanone is excellent. The binding energy value of 126 kJ mol^{-1} (this experiment) is in excellent agreement with a previous HPMS experiment performed by Hoffman which reported a binding energy of 126 kJ mol^{-1} .⁵⁹ The excellent agreement between previous experiments and current theory suggest that the structure of the PBD of butanone is represented by Figure 17, containing one IHB with a binding energy of $126 \pm 2.5 \text{ kJ mol}^{-1}$.

The experimentally obtained entropy values are also in very good agreement with the calculated values. The experimentally determined entropy change is $-144 \pm 10 \text{ J mol}^{-1} \text{ K}^{-1}$ which is very close to the calculated value of $-140 \text{ J mol}^{-1} \text{ K}^{-1}$. The entropy values are also in good agreement with the previous experiment which reported an entropy value of $-128 \text{ J mol}^{-1} \text{ K}^{-1}$.⁵⁹

The agreement of the Gibbs free energy change is very good between the current experiment and the best theoretical calculations performed to date. The experimental ΔG_{298} is $-83.1 \pm 8 \text{ kJ mol}^{-1}$, which agrees well with the calculated ΔG_{298} of $-86.9 \text{ kJ mol}^{-1}$.

The calculated arrangement of the PBD of 2-pentanone shown in Figure 17 represents the experimental values very well. The excellent agreement with previous results and current theory suggests an accurate measurement of the enthalpy and entropy changes in the association reaction of protonated 2-pentanone and its neutral counterpart.

When comparing the butanone PBD formation against the 2-pentanone PBD formation, many similarities are observed. The binding energies are very close in value ($\Delta\Delta H_{\text{rxn}} = \Delta H_{\text{butanone}} - \Delta H_{\text{pentanone}} = -7.7 \text{ kJ mol}^{-1}$). The entropy loss in both systems is near identical ($\Delta\Delta S_{\text{rxn}} = \Delta S_{\text{butanone}} - \Delta S_{\text{pentanone}} = -0.6 \text{ J mol}^{-1} \text{ K}^{-1}$). The butanone system has a stronger binding energy (7.7 kJ mol^{-1} stronger) than the 2-pentanone system but has identical losses of entropy. The loss of entropy would be expected to be comparable between the two systems as the bonding pictures (Figures 15 and 17) show very similar configurations of the atoms. The lower binding energy of the 2-pentanone system is evident when comparing the temperature ranges over which the compounds were able to be studied. The 2-pentanone system covered a temperature range from $141 - 253 \text{ }^{\circ}\text{C}$ while butanone, with a stronger binding energy and same entropy loss, required a temperature range from $193 - 287 \text{ }^{\circ}\text{C}$. The PBD of butanone has a stronger binding energy and thus both monomer and dimer were not able to be formed in the necessary amounts below 193°C while the monomer and dimer of 2-pentanone were observed in good amounts at $141 \text{ }^{\circ}\text{C}$. Conversely, butanone was able to be studied at a higher temperature range than the 2-pentanone system.

3.4 2,4-Pentanedione System

The association reaction involving 2,4-pentandione and protonated 2,4-pentanedione is given by Eq. 37.



The reaction was observed over a temperature range of 130 to 214 °C. Depending on the temperature, between 1 and 40 µL was injected into a heated 5 L stainless steel reservoir. The bath gas for the generation of the 2,4-pentanedione van't Hoff plot was methane, which comprised more than 99% of the total gas mixture.

For a typical experiment the 2,4-pentanedione liquid is injected into the reservoir, allowed to equilibrate for thirty minutes, then the gas mixture is flowed into the ion source. The electronics are then turned on and allowed to equilibrate (≈ 15 minutes) to allow for any electronic drift effects. Time-intensity profiles were collected for m/z 101 and 201 corresponding to the protonated 2,4-pentanedione monomer and dimer, respectively. A van't Hoff plot was generated over $\approx 85^\circ$ temperature range (Figure 18). Using Eq. 17 and 18 the enthalpy and entropy values of the association reaction were obtained. The enthalpy change was determined to be $-118 \pm 2.5 \text{ kJ mol}^{-1}$ and the entropy change was determined to be $-153 \pm 10 \text{ J mol}^{-1} \text{ K}^{-1}$.

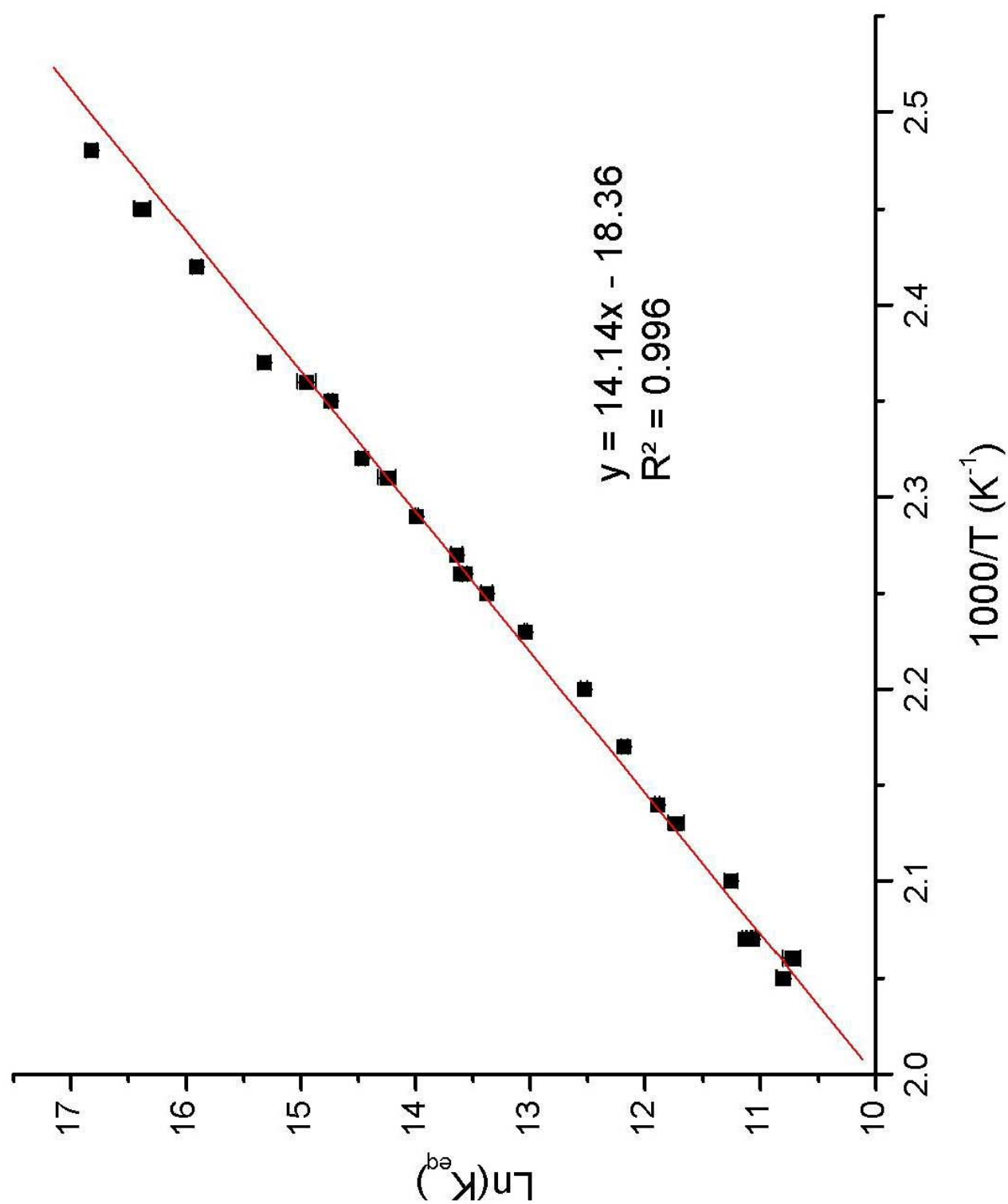


Figure 18 van't Hoff Plot of 2,4-Pentanedione

Electronic structure calculations were performed using a number of different methods. The pentanedione system presented some difficulties not encountered in the mono keto PBDs. The presence of a second carbonyl functional group promotes a tautomerization to the enol form of 2,4-pentanedione. The keto and enol tautomers of 2,4-pentanedione form an equilibrium mixture in solution and therefore there is a mixture of starting products upon the PBD formation of 2,4-pentanedione. The possibility of different isomers as reactants leads to different isomeric possibilities for the PBD. Electronic structure calculations are invaluable in narrowing down the structural possibilities.

As mentioned above, 2,4-pentanedione exists as a mixture of tautomers. At room temperature the keto and enol forms of 2,4-pentanedione are present in a ratio of roughly 15:85, respectively.^{61,62} This equilibrium shifts to 66 ± 5 % enol at 105 °C.⁶² This suggests that a mixture of isomers is present as neutral reactants in the PBD formation of 2,4-pentanedione.

Electronic structure calculations can be used to determine minimum energy structures, which is necessary for the computational determination of ΔH_{rxn} and ΔS_{rxn} . The equilibrium of the neutral forms of 2,4-pentanedione is shown below (Figure 19).

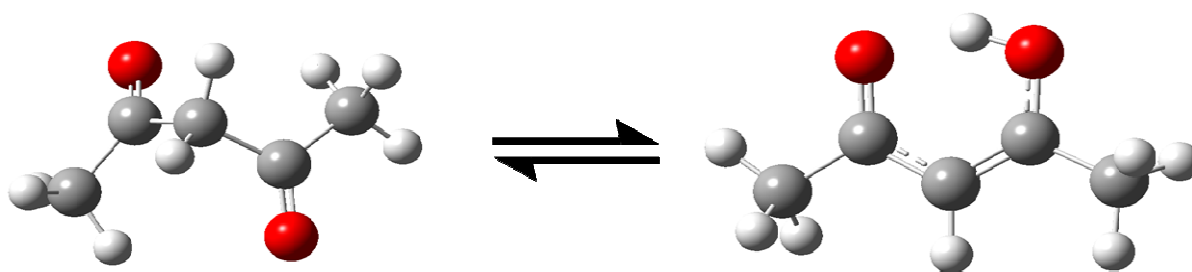


Figure 19 G3(MP2) Optimized Structures of the Keto-Enol Equilibrium of 2,4-Pentanedione

The abundance of the keto and enol isomers can be determined based on the relative stabilities of the different isomers. Based on the Gibbs free energy of the two tautomers, the equilibrium constant can be calculated at a given temperature (see Eq. 14). Since the experiment covers an 85 ° temperature range, the proportions of keto to enol tautomers changes. At all points along the temperature range the enol form of 2,4-pentanedione is favoured. At the lowest experimental temperature (130 °C) ΔG_{rxn} (Figure 19) is -7 kJ mol⁻¹ as calculated by the G3(MP2) method. A ΔG_{rxn} of -7 kJ mol⁻¹ gives an equilibrium constant at 130 °C of 16. The ΔG_{rxn} ranges from -7 kJ mol⁻¹ at 130 °C to -5 kJ mol⁻¹ at 214 °C, yielding an equilibrium constant at 214 °C of 3.4. At all temperatures, the G3(MP2) calculations predict a gas composition that is heavily dominated by the enol tautomer. This has been well established in previous studies.^{58,63}

A closer look at the enol form of 2,4-pentanedione displays why the enol form is favoured. The enol form is resonance stabilized and contains a strong intramolecular hydrogen bond. The keto form has no resonance stabilization and contains very weak intramolecular hydrogen bonds. If only absolute entropy is considered, the keto form is favoured by 17 J mol⁻¹ K⁻¹, as determined by G3(MP2) calculations. The keto form of 2,4-pentanedione contains no intramolecular hydrogen bond. The intramolecular hydrogen bond in the enol form restricts the internal rotation, resulting in a tighter structure and fewer degrees of freedom than that of the keto structure.

Considered next are the relative stabilities of the protonated forms of 2,4-pentanedione. The protonated keto and enol forms are presented in Figure 20.

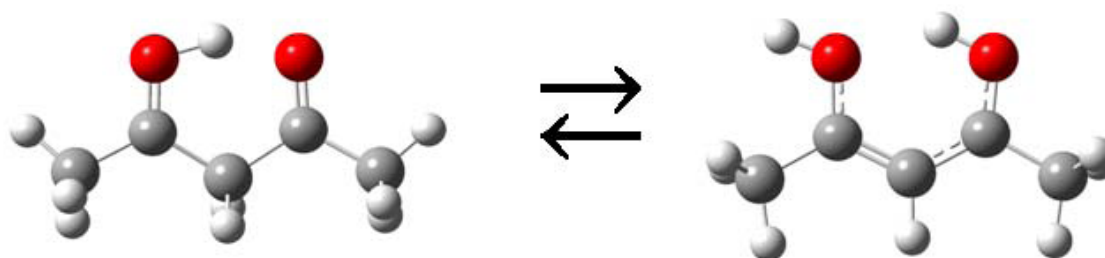


Figure 20 G3(MP2) Optimized Structures of the Keto-Enol Equilibrium of Protonated 2,4-Pentanedione

When comparing the absolute Gibbs free energy of the enol form against the keto form of protonated 2,4-pentanedione, the enol form is favoured by 17 kJ mol^{-1} . Again the enol form is able to effectively delocalize the positive charge through resonance stabilization while the keto form cannot. The absolute entropy of the protonated keto form is favoured by only $7 \text{ J mol}^{-1} \text{ K}^{-1}$ as the keto form now also possesses an intramolecular ionic hydrogen bond which restricts the internal rotation. Even at the highest temperature point achieved during the experiment (214°C), which favours the keto structure, the equilibrium constant of Figure 20 has a value of 66, suggesting a mass spectrum dominated by protonated enol tautomer of 2,4-pentanedione.

Next considered are the proton bound dimers of 2,4-pentanedione. Three possible structures of the PBD of 2,4-pentanedione have been identified so far (Figure 21).

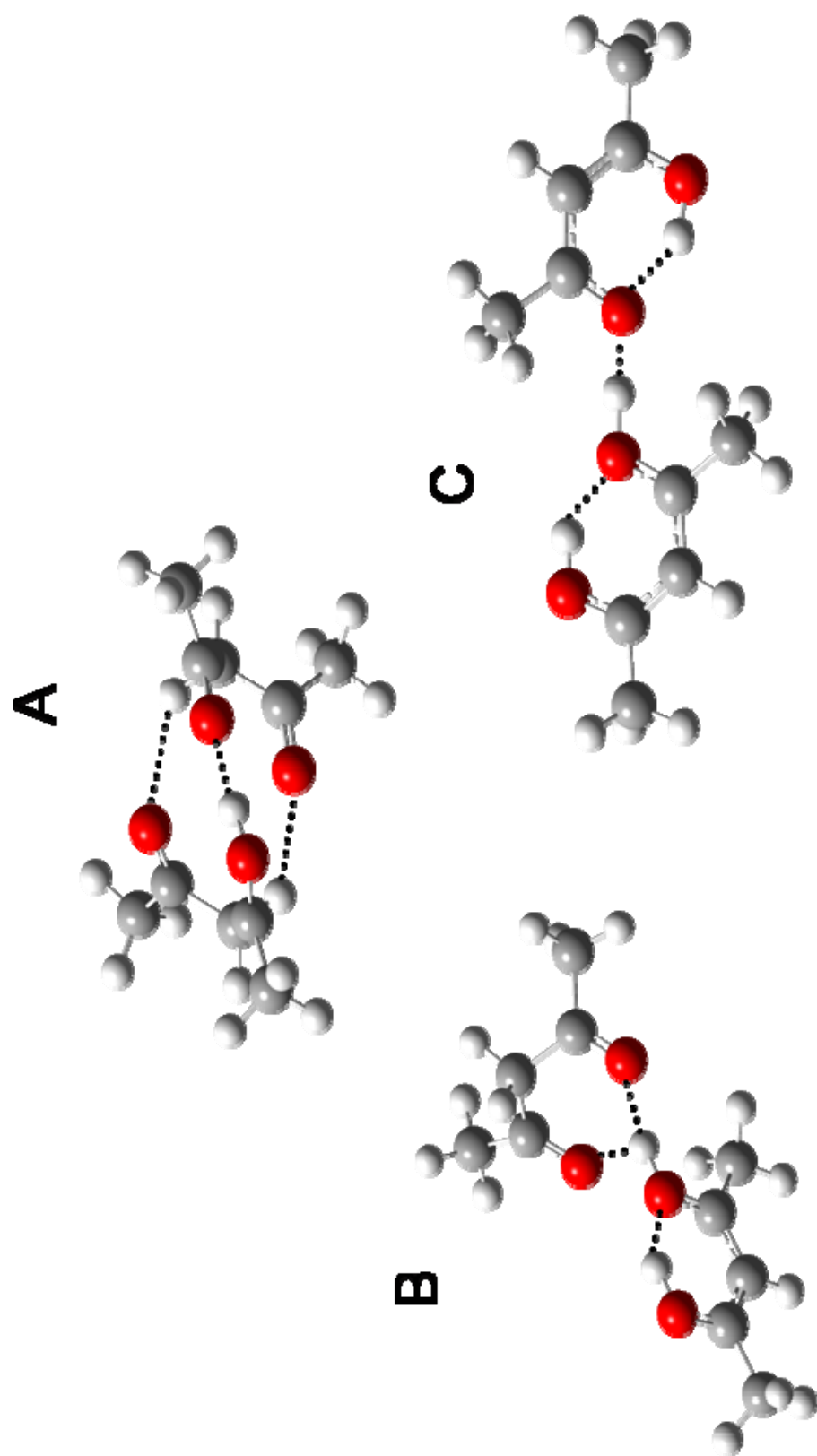


Figure 21 MP2(Full)/6-311+G(d,p)//MP2(Full)6-31G(d) Optimized Structures of the PBD of 2,4-Pentanedione

Of the structures displayed in Figure 21 only two are probable configurations of the PBD of 2,4-pentanedione. Structure A, termed the keto-keto isomer, contains 3 intermolecular hydrogen bonds with one being an ionic hydrogen bond. However, isomer A is too high in free energy when compared with the other isomers and can be effectively eliminated. Isomers B and C, termed the keto-enol and enol-enol isomers, respectively, are the lowest energy structures determined. In terms of stabilities of the isomers of B and C, the enol-enol or C isomer is the most stable. The enol-enol isomer contains three hydrogen bonds, one ionic and two intramolecular. Conversely, the B isomer, or the keto-enol isomer contains only two hydrogen bonds and is lacking an intramolecular hydrogen bond that the enol-enol isomer possesses.

The reactions that most closely matched experiment are shown in Figures 22 – 24 and the thermochemical data is summarized in Table 4. All calculations for Figures 22 - 24 were performed using the MP2(Full)/6-311+G(d,p)//MP2(Full)/6-31G(d) method for geometry optimization and single point determination.

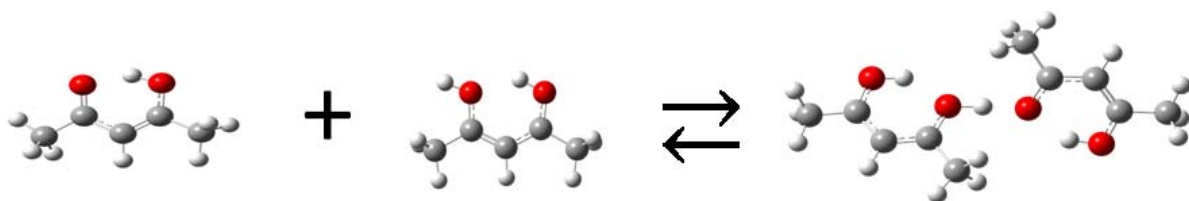


Figure 22 **Reaction Scheme A1- Enol-Enol PBD of 2,4-Pentanedione**

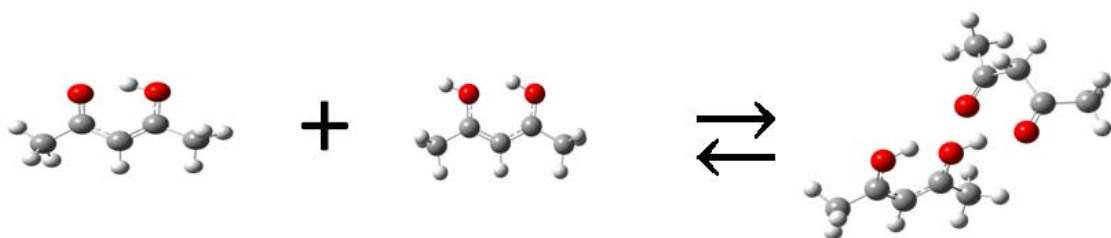


Figure 23 **Reaction Scheme A2 - Keto-Enol PBD of 2,4-Pentanedione**

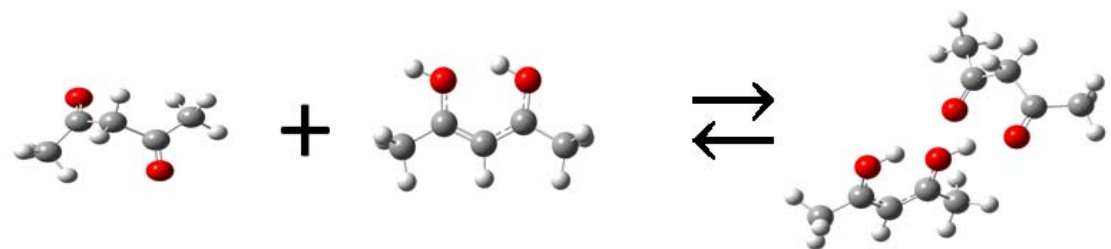


Figure 24 **Reaction Scheme A3 – Keto-Enol PBD of 2,4-Pentanedione**

Table 5 2,4-Pentanedione Thermochemical Data, Experimental and Calculated Summary

Source	ΔH (kJ mol ⁻¹) (kcal mol ⁻¹)	ΔS (J mol ⁻¹ K ⁻¹) (cal mol K ⁻¹)	ΔG (kJ mol ⁻¹) (kcal mol ⁻¹)
Current HPMS Experiment	-117.6 (-28.1)	-152.7 (-36.5)	-72.1 (-17.2)
Reaction Scheme A1	-118.1 (-28.2)	-131.6 (-31.5)	-78.9 (-18.8)
Reaction Scheme A2	-113.6 (-27.2)	-134.8 (-32.2)	-73.4 (-17.5)
Reaction Scheme A3	-119.9 (-28.7)	-144.4 (-34.5)	-76.8 (-18.4)

All three reaction schemes produce results that are in very good agreement with the experimental determination of the enthalpy and entropy change for the formation of the PBD of 2,4-pentanedione. Reaction scheme A1 matches the experimental enthalpy change of -118 ± 2.5 kJ mol⁻¹ almost exactly. The bonding scheme proposed in A1 is the neutral enol form of 2,4-pentanedione associating with the protonated enol form of 2,4-pentanedione to form the enol-enol PBD. This reaction seems the most likely as the majority of the gas phase reactants exist in the enol form to begin with. Reaction schemes A2 and A3 are also very close to the experimental enthalpy change with binding energies of 114 and 120 kJ mol⁻¹, respectively. Reaction scheme A2 involves the enol reactants forming a keto-enol cluster. In order to achieve the product seen in reaction scheme A2 an isomerisation must occur upon association of the two reactants. Reaction scheme A3 more closely matches the experimental enthalpy change and requires no isomerisation upon association of the reactants. Reaction scheme A3 involves the protonated enol form of 2,4-pentanedione reacting with the neutral keto form of 2,4-pentanedione to produce the keto-enol version of the PBD. All three reaction schemes are possible and most likely a combination of these schemes is occurring during the experiment.

The entropy loss determined by the HPMS experiment for the formation of the PBD of 2,4-pentanedione is -153 ± 10 J mol⁻¹ K⁻¹. This value is more negative than any of the calculated entropy changes, however, the theoretical entropy changes are close in value. Reaction scheme

A1 produces the most positive entropy change of all the theoretical calculations presented here. The value as determined by scheme A1 is $-132 \text{ J mol}^{-1} \text{ K}^{-1}$ and is the value furthest away from the experimental value. The most positive entropy change is indicative of the 'loosest' calculated structure. Both reaction schemes A2 and A3 produce the slightly more restricted keto structures, and as a result have slightly more negative entropy changes. The closest match to the experimental entropy change for the PBD formation of 2,4-pentanedione is reaction scheme A3. Reaction scheme A3 has an entropy change of $-144 \text{ J mol}^{-1} \text{ K}^{-1}$, which is in very good agreement with the experimentally determined value of $-153 \pm 10 \text{ J mol}^{-1} \text{ K}^{-1}$.

The last quantity to consider at this point is the Gibbs free energy change. The experimental value is $-72 \pm 2.5 \text{ kJ mol}^{-1}$ at 298 K. Again all three Gibbs free energy changes for the calculated reaction schemes are in very good agreement with the experimental value. The closest match to the value determined by the HPMS experiment is reaction scheme A2, with a value of -73 kJ mol^{-1} at 298 K.

It is difficult to assign one particular reaction scheme to the association reaction forming the PBD of 2,4-pentanedione. Most likely a combination of these reactions is occurring at any one time during the experiment. The composition of the keto to enol equilibrium is a function of temperature, therefore ensuring a higher composition of loose structures at higher temperatures and tighter structures at lower temperatures.

3.5 1,1,1-Trifluoro 2,4 pentanedione system

The association reaction involving 1,1,1-trifluoro-2,4-pentanedione and protonated 1,1,1-trifluoro-2,4-pentanedione is given by Eq. 38.



The reaction was observed over a temperature range of 42 to 120 °C. Depending on the temperature between 1 and 40 μL was injected into a heated 5 L stainless steel reservoir. The bath gas for the generation of the 1,1,1-trifluoro-2,4-pentanedione van't Hoff plot was methane, which comprised more than 99% of the total gas mixture.

For a typical experiment the 1,1,1-trifluoro-2,4-pentanedione liquid is injected into the reservoir and allowed to equilibrate for thirty minutes before the gas mixture is flowed into the ion source. The electronics are then turned on and allowed to equilibrate (≈ 15 minutes) to allow for any electronic drift effects. Time-intensity profiles were collected for m/z 155 and 309 corresponding to the protonated 1,1,1-trifluoro-2,4-pentanedione monomer and dimer, respectively. A van't Hoff plot was generated over $\approx 80^\circ$ temperature range (Figure 25). Using Eq. 17 and 18 the enthalpy and entropy values of the association reaction were obtained. The enthalpy change was determined to be $-162 \pm 2.5 \text{ kJ mol}^{-1}$ and the entropy change was determined to be $-317 \pm 10 \text{ J mol}^{-1} \text{ K}^{-1}$.

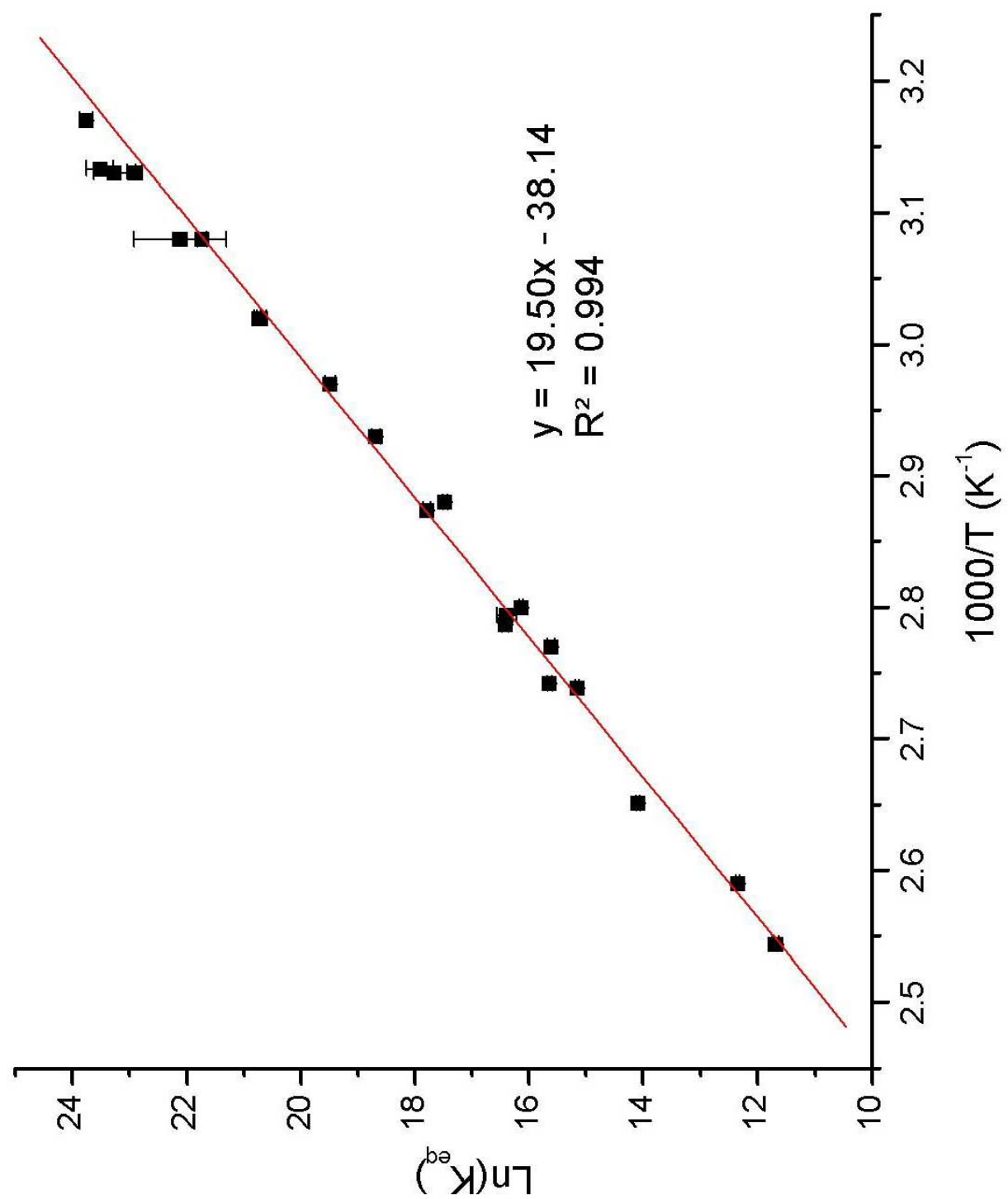


Figure 25 van't Hoff Plot of 1,1,1-Trifluoro-2,4-Pentanedione

Electronic structure calculations were performed using a number of different methods. The 2,4-pentanedione system contained a mixture of keto and enol isomers. With 1,1,1-trifluoro-2,4-pentanedione the isomeric ratio of keto to enol isomers is calculated to be shifted heavily to the enol side. The keto to enol equilibrium of 1,1,1-trifluoro-2,4-pentanedione is shown in Figure 26 as calculated using the G3(MP2) method.

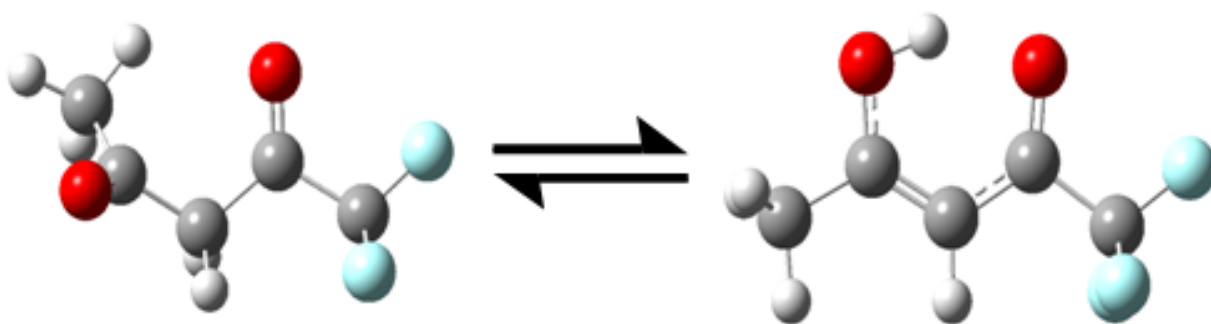


Figure 26 Keto-Enol Equilibrium of 1,1,1-Trifluoro-2,4-Pentanedione

The presence of the trifluoro group shifts the equilibrium displayed in Figure 26 far to the right. The enol form of 1,1,1-trifluoro-2,4-pentanedione is favoured enthalpically by 22 kJ mol^{-1} over the keto form. This is attributed to the presence of the intramolecular hydrogen bond as well as the resonance stabilization that the molecule is able to achieve in this isomeric form. Conversely, the keto form of the molecule is favoured entropically by $21 \text{ J mol}^{-1} \text{ K}^{-1}$. Overall, the Gibbs free energy change of the reaction presented in Figure 26 is $-15.9 \text{ kJ mol}^{-1}$. This yields a value for the equilibrium constant of 130 at 120°C , the highest temperature reached in these experiments. Essentially, very little of the keto tautomer is expected to exist as a neutral reactant in the formation reaction of 1,1,1-trifluoro-2,4-pentanedione PBD.

Considered next are the corresponding protonated forms of the keto and enol tautomers of 1,1,1-trifluoro-2,4-pentanedione. As in the case of 2,4-pentanedione, upon protonation the enol form is favoured even more. Figure 27 displays the keto to enol equilibrium of protonated 1,1,1-trifluoro-2,4-pentanedione as calculated by the G3(MP2) method.

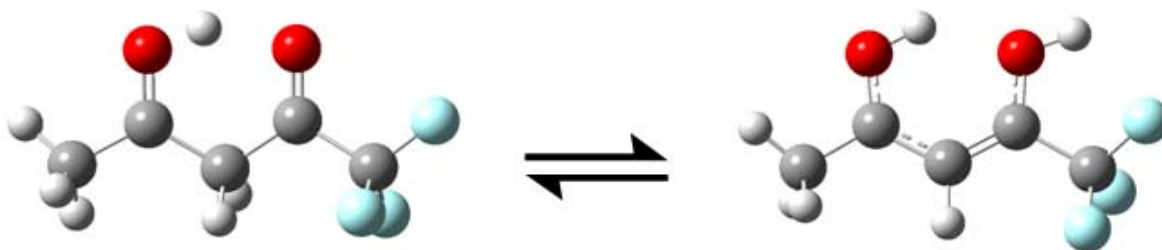


Figure 27 Keto-Enol Equilibrium of Protonated 1,1,1-Trifluoro-2,4-Pentanedione

In the case of the protonated tautomers of 1,1,1-trifluoro-2,4-pentanedione the enthalpy change for the keto to enol tautomerism is quite close to the enthalpy change seen in the neutral species. The protonated enol form of 1,1,1-trifluoro-2,4-pentanedione is favoured by 24 kJ mol^{-1} over the keto form, whereas the enol is favoured by 22 kJ mol^{-1} in the corresponding neutral reaction, in terms of absolute enthalpy. The major difference seen in the protonated keto to enol equilibrium is the presence of an intramolecular hydrogen bond in the keto structure which restricts the rotation of the carbonyl groups. This restriction results in the keto form having a comparable absolute entropy to that of the enol form. The keto form is favoured in terms of entropy by $1 \text{ J mol}^{-1} \text{ K}^{-1}$. This leads to a Gibbs free energy change of -23 kJ mol^{-1} for the reaction shown in Figure 27. At the highest experimental temperature of 120°C the value for the equilibrium constant for the keto-enol equilibrium of 1,1,1-trifluoro-2,4-pentanedione is ≈ 1200 .

The gas phase reactants for the formation of 1,1,1-trifluoro-2,4-pentanedione PBD are expected to be essentially all in the enol form with very little keto tautomer present. Figure 28 displays the most likely formation of the PBD of 1,1,1-trifluoro-2,4-pentanedione calculated as of now.

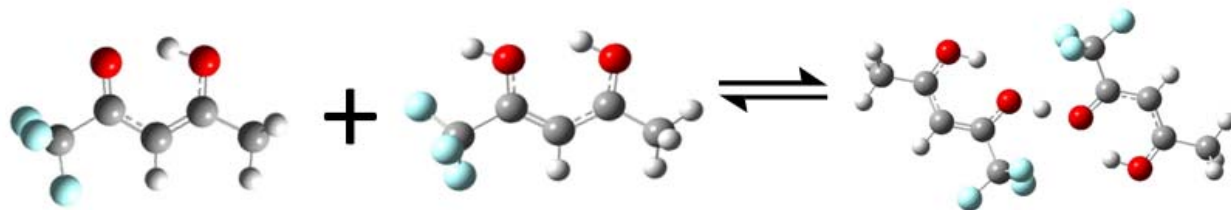


Figure 28 Most Likely PBD Formation of 1,1,1-Trifluoro-2,4-Pentanedione as Calculated by B3LYP/6-311++G(2DF,2PD)//B3LYP/6-31G(d)

Table 6 displays the results of the experimental and theoretical results for the formation reaction of the PBD of 1,1,1-trifluoro-2,4-pentanedione.

Table 6 1,1,1-trifluoro-2,4-Pentanedione Thermochemical Data, Experimental and Calculated Summary

Source	ΔH (kJ mol ⁻¹) (kcal mol ⁻¹)	ΔS (J mol ⁻¹ K ⁻¹) (cal mol K ⁻¹)	ΔG (kJ mol ⁻¹) (kcal mol ⁻¹)
Current HPMS Experiment	-162.1 (-38.8)	-317.1 (-75.8)	-67.6 (-16.2)
B3LYP/6-311++G(2df,2pd)// B3LYP/6-31G(d)	-108.3 (-25.9)	-153.2 (-36.6)	-62.6 (-15.0)
MP2(FULL)/6-311+G(d,p)// B3LYP/6-31G	-107.6 (-25.7)	-162.6 (-38.9)	-59.1 (-14.1)

Immediately a very large discrepancy is noticed between the theoretical predictions and experimental evidence. The current calculations are therefore not likely representative of what is occurring during the experiment. The experimental data suggest a much stronger binding energy and much larger loss of entropy than the calculations predict, most likely a covalently bound species. Numerous association reactions have been calculated using a variety of methods and different structures; however, currently these are the best calculated reactions for this system. The experiment was performed below 125 °C. Above 125 °C poor signal intensity prevented the collection of reliable time-intensity profiles.

The discrepancy between theory and experiment has not been resolved. Further investigation into the 1,1,1-trifluoro-2,4-pentanedione system is warranted.

3.6 1,1,1,5,5,5-Hexafluoro-2,4-Pentanedione System

The association reaction involving 1,1,1,5,5,5-hexafluoro-2,4-pentanedione and protonated 1,1,1,5,5,5-hexafluoro-2,4-pentanedione is given by Eq. 39.



The reaction was observed over a temperature range of 38 to 93 °C. Depending on the temperature, between 2 and 150 µL was injected into a heated 5 L stainless steel reservoir. The bath gas for the generation of the 1,1,1,5,5,5-hexafluoro-2,4-pentanedione van't Hoff plot was methane, which comprised more than 99% of the total gas mixture.

For a typical experiment the 1,1,1,5,5,5-hexafluoro-2,4-pentanedione liquid is injected into the reservoir allowed to equilibrate for thirty minutes before the gas mixture is flowed into the ion source. The electronics are then turned on and allowed to equilibrate (≈ 15 minues) to allow for any electronic drift effects. Time-intensity profiles were collected for m/z 209 and 417 corresponding to the protonated 1,1,1,5,5,5-hexafluoro-2,4-pentanedione monomer and dimer, respectively. A van't Hoff plot was generated over $\approx 55^\circ$ temperature range (Figure 29). Using Eq. 17 and 18 the enthalpy and entropy values of the association reaction were obtained. The enthalpy change was determined to be $-121 \pm 2.5 \text{ kJ mol}^{-1}$ and the entropy change was determined to be $-260 \pm 10 \text{ J mol}^{-1} \text{ K}^{-1}$.

Electronic structure calculations were performed using a variety of methods. The keto-enol equilibrium of 1,1,1,5,5,5-hexafluoro-2,4-pentanedione was examined based on the relative stabilities of the two tautomers. Figure 30 displays the tautomerization of 1,1,1,5,5,5-hexafluoro-2,4-pentanedione as calculated by the G3(MP2) method.

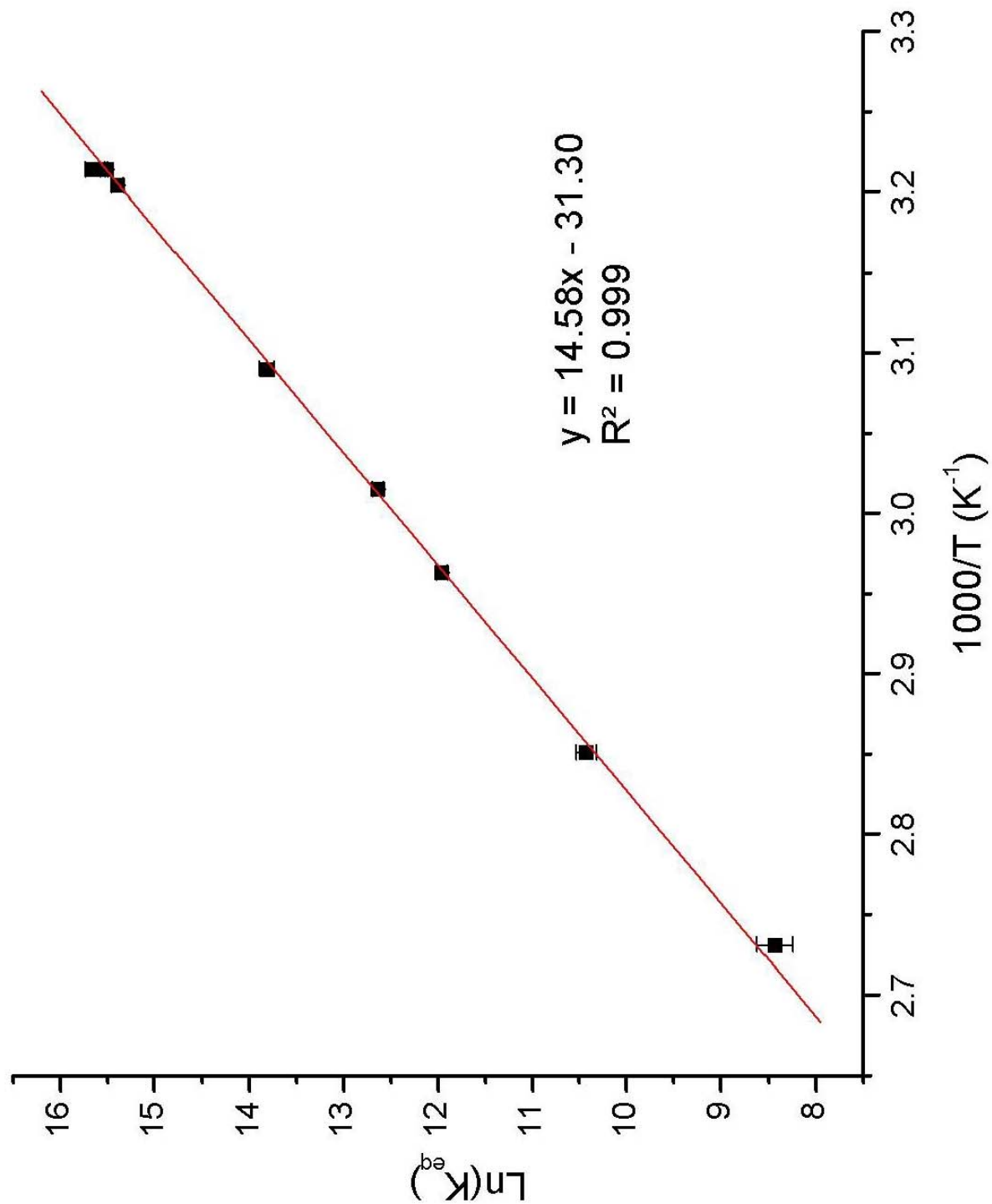


Figure 29 van't Hoff Plot of 1,1,1,5,5,5-Hexafluoro-2,4-Pentanedione



Figure 30 Keto-Enol Equilibrium of Protonated 1,1,1,5,5,5-Hexafluoro-2,4-Pentanedione

The Gibbs free energy change for the reaction displayed in Figure 31 is -35 kJ mol^{-1} as calculated by the G3(MP2) method. This free energy change yields an equilibrium constant of ≈ 10000 at 93°C . Based on the relative stabilities, the enol form of neutral and protonated 1,1,1,5,5,5-hexafluoro-2,4-pentanedione should essentially be the only tautomer present.

Based on the relative energies of the hexafluorinated pentanedione species a most likely reaction scheme can be presented. Figure 32 shows the most likely scheme of the association reaction forming the PBD of 1,1,1,5,5,5-hexafluoro-2,4-pentanedione.

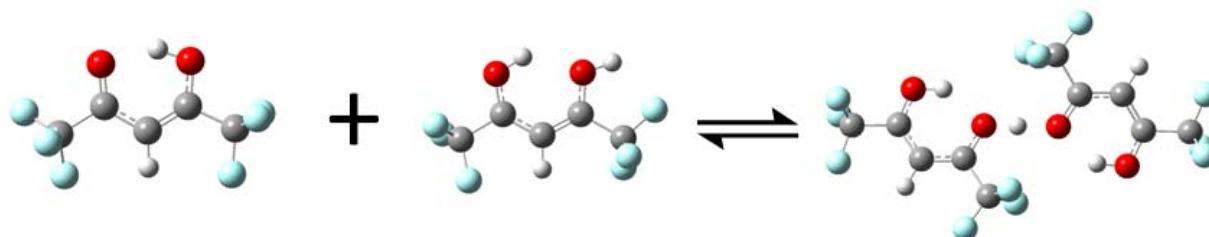


Figure 31 Most Likely PBD Formation of 1,1,1,5,5,5-Hexafluoro-2,4-Pentanedione as Calculated by MP2(Full)/6-311+G(d,p)//B3LYP/6-31G(d)

The values obtained from the reaction scheme presented in Figure 32 are summarized in Table 7.

Table 7 1,1,1,5,5,5,-Hexafluoro-2,4-Pentanedione Thermochemical Data, Experimental and Calculated Summary

Source	ΔH (kJ mol ⁻¹) (kcal mol ⁻¹)	ΔS (J mol ⁻¹ K ⁻¹) (cal mol K ⁻¹)	ΔG (kJ mol ⁻¹) (kcal mol ⁻¹)
Current HPMS Experiment	-121.2 (-29.0)	-260.2 (-62.2)	-43.6 (-10.4)
MP2(FULL)/6-311+G(d,p)// B3LYP/6-31G(d)	-99.6 (-20.6)	-152.6 (-31.5)	-54.1 (-11.2)
B3LYP/6-311++G(2df,2pd)// B3LYP/6-31G(d)	-87.1 (-20.8)	-153.2 (-36.6)	-41.4 (-9.9)

The experimental value of the enthalpy of the reaction is -121 ± 2.5 kJ mol⁻¹. The theoretical reaction depicted in Figure 32. The corresponding ΔH and ΔS summarized in Table 7 are not in good agreement with the experimental data. The closest calculation using the MP2(Full)/6-311+G(d,p)//B3LYP/6-31G(d) method, yields a value for the enthalpy of reaction of -100 kJ mol⁻¹. The closest calculated value is 21 kJ mol⁻¹ lower than the experimentally determined value and based on this alone it is evident that the reaction scheme presented in Figure 32 is not representative of the reaction observed during the experiment.

Another discrepancy between the values obtained by calculations for the reaction scheme of Figure 32 and the experimental values is the large difference in the entropy change. The experimental value is -260 ± 10 J mol⁻¹ K⁻¹ indicating decreased internal degrees of freedom and increased steric effects that are not represented by the current reaction scheme, which gives an entropy loss of -153 J mol⁻¹ K⁻¹ as calculated by both methods.

The reaction depicted in Figure 32 is the most likely reaction based on the argument of the relative stabilities of the molecules mentioned above. Other reactions can be envisaged using products and reactants of 1,1,1,5,5,5-hexafluoro-2,4-pentanedione that are not the lowest in absolute energy and therefore not the most stable species (Figures 33-35).

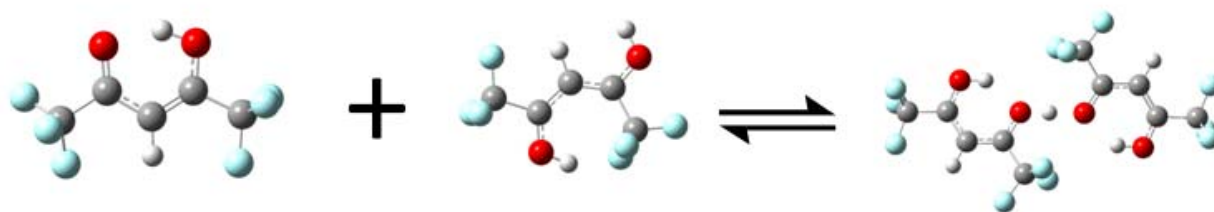


Figure 32 Reaction Scheme B1 for 1,1,1,5,5,5-Hexafluoro-2,4-Pentanedione

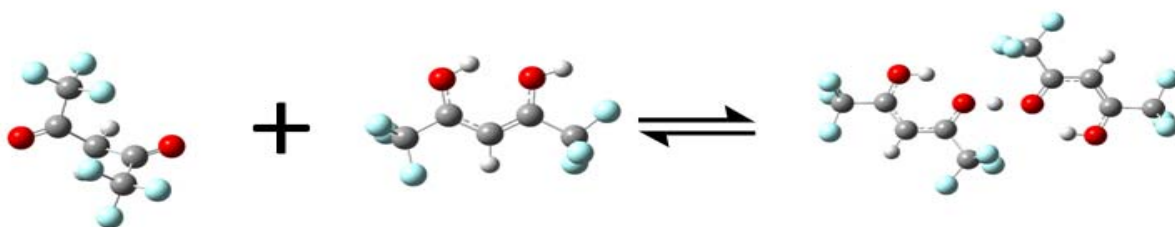


Figure 33 Reaction Scheme B2 for 1,1,1,5,5,5-Hexafluoro-2,4-Pentanedione



Figure 34 Reaction Scheme B3 for 1,1,1,5,5,5-Hexafluoro-2,4-Pentanedione

Table 8 Summary of Reaction Schemes B1-B3 for 1,1,1,5,5,5-Hexafluoro-2,4-Pentanedione

Source	ΔH (kJ mol ⁻¹) (kcal mol ⁻¹)	ΔS (J mol ⁻¹ K ⁻¹) (cal mol K ⁻¹)	ΔG (kJ mol ⁻¹) (kcal mol ⁻¹)
Current HPMS Experiment	-121.2 (-29.0)	-260.2 (-62.2)	-43.6 (-10.4)
Reaction Scheme B1	-126.7 (-30.3)	-141.5 (-33.8)	-84.5 (-20.2)
Reaction Scheme B2	-115.8 (-27.7)	-160.3 (-38.3)	-68.0 (-16.3)
Reaction Scheme B3	-123.5 (-29.5)	-154.1 (-36.8)	-77.5 (-18.5)

The reaction schemes presented in Figure 33 – 35 were performed at the MP2(FULL)/6-311+G(d,p)//B3LYP/6-31G level of theory. In each reaction scheme (B1-B3) one of the participants in the reaction is not the most stable structure. The calculated enthalpy changes are in much better agreement with the experimental value, however, the entropy changes are still vastly different. The thermochemical information for Figures 33 – 35 is summarized in Table 8.

Figure 33 presents reaction scheme B1, involving a different protonated monomer than that considered in Figure 32. The protonated monomer is slightly higher in energy compared to the lowest energy structure for protonated monomers. The lowest energy structure is favoured by 27 kJ mol⁻¹ in terms of absolute enthalpy. However, reaction scheme B1 produces an overall enthalpy of reaction of -127 kJ mol⁻¹, bringing the value close to the experimental value. Reaction B1 would require an isomerisation during the association reaction to form the PBD. The entropy change determined in reaction B1 is very similar to the change determined for the most likely reaction (Figure 32). All current calculations report similar entropy changes ($\approx 140 - 160$ J mol⁻¹ K⁻¹) which are considerably different from the experimental value of -260 ± 10 J mol⁻¹ K⁻¹.

Figure 34 involves the keto form of 1,1,1,5,5,5-hexafluoro-2,4-pentanedione as the neutral reactant. As mentioned above it is unlikely that much of the keto form is present in the ion source. The enthalpy change for reaction scheme B2 (Figure 34) is -116 kJ mol⁻¹.

Figure 35 involves a slightly different form of the PBD of 1,1,1,5,5,5-hexafluoro-2,4-pentanedione. The PBD shown in reaction scheme B3 is not the most stable structure for the PBD of 1,1,1,5,5,5-hexafluoro-2,4-pentanedione but it is a possible structure. The most stable isomer of the PBD of 1,1,1,5,5,5-hexafluoro-2,4-pentanedione is shown in Figure 32 and is favoured in terms of absolute enthalpy over the PBD form seen in Figure 35 by 29 kJ mol^{-1} . Again, this structure is not expected to be prevalent in the source. Forms other than the PBD of 1,1,1,5,5,5-hexafluoro-2,4-pentanedione have been investigated including some covalent structures (Figure 36).

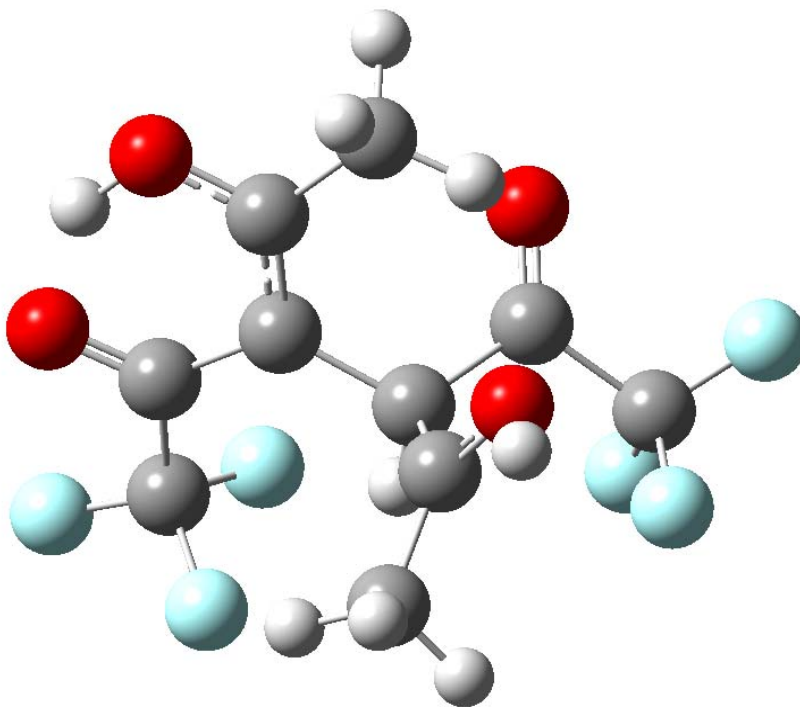


Figure 35 **Possible Covalent Structure of 1,1,1,5,5,5-Hexafluoro-2,4-Pentanedione**

Currently all calculated covalent structure reaction schemes are heavily endothermic and do not seem possible as representative of the process occurring during the experiment.

It is thus evident that the current calculations do not represent the process occurring during the experiment. The experimental data exhibits a very pronounced temperature dependence as evidenced by the very large entropy loss. The calculations do not mimic this behaviour. The experiment was performed at very low temperatures ($< 100\text{ }^{\circ}\text{C}$) as above these temperatures poor signal intensity prevented measurements from being taken.

The discrepancy between the experiment and theory has not been resolved. Further investigation into the 1,1,1,5,5,5-hexafluoro-2,4-pentanedione system is warranted.

3.7 Conclusion

Hydrogen bonding has been explored using the simple mono-ketones of butanone and 2-pentanone. Expected binding energies and bonding arrangements of the proton bound dimers of the mono-ketones are observed. Experimental binding energies in the range from 125 – 135 kJ mol⁻¹ are in very good agreement with the calculated binding energies.

Hydrogen bonding and the effect of fluorinating 2,4-pentanedione has also been investigated using the more complex β -diketones of 2,4-pentanedione, 1,1,1-trifluoro-2,4-pentanedione and 1,1,1,5,5,5-hexafluoro-2,4-pentanedione. β -diketones exist as an equilibrium mixture of keto and enol isomers. The experimental enthalpy and entropy of reaction for the formation of the proton bound dimer of 2,4-pentanedione most likely contains a mixture of keto and enol isomers whose composition changes with temperature. The calculated binding energies and entropy losses correspond well with the experimental values.

The effects of fluorinating 2,4-pentanedione are still to be determined. It is expected that the tri- and hexa- fluorinated 2,4-pentanedione species exist essentially as enol tautomers in the gas phase association reactions. However, current calculations predict a much weaker binding

energy and entropy loss than that observed experimentally. The calculations presented here for the tri- and hexa- fluorinated 2,4-pentanedione experiments are not representative of what is occurring during experiment.

4.0 Sodiated Clusters

4.1 *Introduction to Sodiated Clusters*

Sodium, the most abundant alkali metal, is prevalent in many areas of active scientific research. In biological systems the sodium cation participates in enzyme regulation and transmembrane transport processes.⁶⁴ The sodium cation is ubiquitous in aqueous chemistry, being a major contributor to the ionic strength of seawater. The interest in the sodium cation also extends into the gas phase as biological applications of mass spectrometry often involve sodium cation complexes.⁶⁵⁻⁶⁷ The gas phase participation of the sodium cation is not limited to biological applications alone as the sodium ion is also postulated to be involved in the formation of metal containing molecules in various astrophysical environments.^{68,69} The wide range of sodiated gas phase complexes necessitates a solid understanding of the structure and energetics of sodium cation binding to small molecules.

Many studies have been devoted to the gas-phase thermochemistry of the sodium cation. Recently, a number of review papers have been published regarding the gas-phase binding energetics of sodium cations with small organic molecules.⁷⁰⁻⁷⁴ The review papers have evaluated the gas phase sodium cation affinity (SCA) scale. The SCA is defined as the negative enthalpy change of the association reaction involving the sodium cation and a small molecule. Absolute values of SCAs can be determined using HPMS. A number of other techniques are able to determine relative SCAs. Recent publications by Bloomfield et al. evaluated the relative and absolute sodium free energy changes against novel ‘model chemistry’ composite computational techniques.^{75,76} The computational technique that was used was CP-dG2thaw, a variation of Gaussian 2 theory (G2).⁷⁷ The CP-dG2thaw technique is a specialized tool tailored for

calculations on molecules and molecular ions involving one or more metal ions.⁷⁶ The results of the evaluation by Bloomfield et al.⁷⁶ concluded that the theoretical method is consistent with the relative free energy changes obtained by McMahon and Ohanessian.⁷¹ McMahon and Ohanessian performed Fourier Transform Ion Cyclotron Resonance Mass Spectrometry (FT-ICR-MS) ligand exchange equilibrium experiments to establish a relative scale of sodium binding free energies.⁷¹ In order to construct an absolute scale, it is necessary to choose at least one compound of sodium ion binding free energy that has been determined absolutely. HPMS experiments give accurate free energy changes.⁷¹ McMahon and Ohanessian anchored the values to the methylamine free energy change as determined through HPMS by Hoyau et al.⁷⁰ The agreement between the theoretical calculations and the *relative* free energy changes is excellent. The *absolute* experimental ladder is reported to be still open to question. Bloomfield et al.⁷⁶ report a modest disagreement between experiment and theory. The CP-dG2thaw sodium ion/ligand bond strengths are clustered $2.1 \pm 1.1 \text{ kJ mol}^{-1}$ higher than the experimental values which are anchored to the $\text{Na}^+/\text{CH}_3\text{NH}_2$ binding energy determined by HPMS.

Absolute binding energies of sodium cation complexes have been investigated for several key functional groups, however, the coverage has by no means been exhaustive. The ability to determine absolute binding energies is the strength of the HPMS experiments. The following studies have been undertaken to contribute to the database of thermochemical information regarding the sodium cation.

4.2 Diethylether Results and Discussion

The association reaction involving diethylether and the sodium cation is given in Eq. 40.



The reaction was observed over a temperature range of 190 to 335 °C. Depending on the temperature, between 1 and 50 μL of diethylether (Et_2O) was injected into a heated 5 L stainless steel reservoir. The bath gas for the generation of the $\text{Na-Et}_2\text{O}^+$ van't Hoff plot was nitrogen, which comprised more than 99% of the total gas mixture.

For a typical experiment the diethylether liquid is injected into the reservoir and allowed to equilibrate for thirty minutes. The gas mixture then is flowed into the ion source and allowed to pick up the sodium vapour. The electronics are then turned on and allowed to equilibrate (≈ 15 minutes) to allow for any electronic drift effects. Time intensity profiles were collected for m/z 23 and 97 corresponding to the sodium cation and $\text{Na-Et}_2\text{O}^+$, respectively. A van't Hoff plot was generated over $\approx 145^\circ$ temperature range (Figure 37). Using Eq. 17 and 18 the enthalpy and entropy values of the association reaction were obtained. The enthalpy change was determined to be $-137 \pm 2.5 \text{ kJ mol}^{-1}$ and the entropy change was determined to be $-130 \pm 10 \text{ J mol}^{-1} \text{ K}^{-1}$.

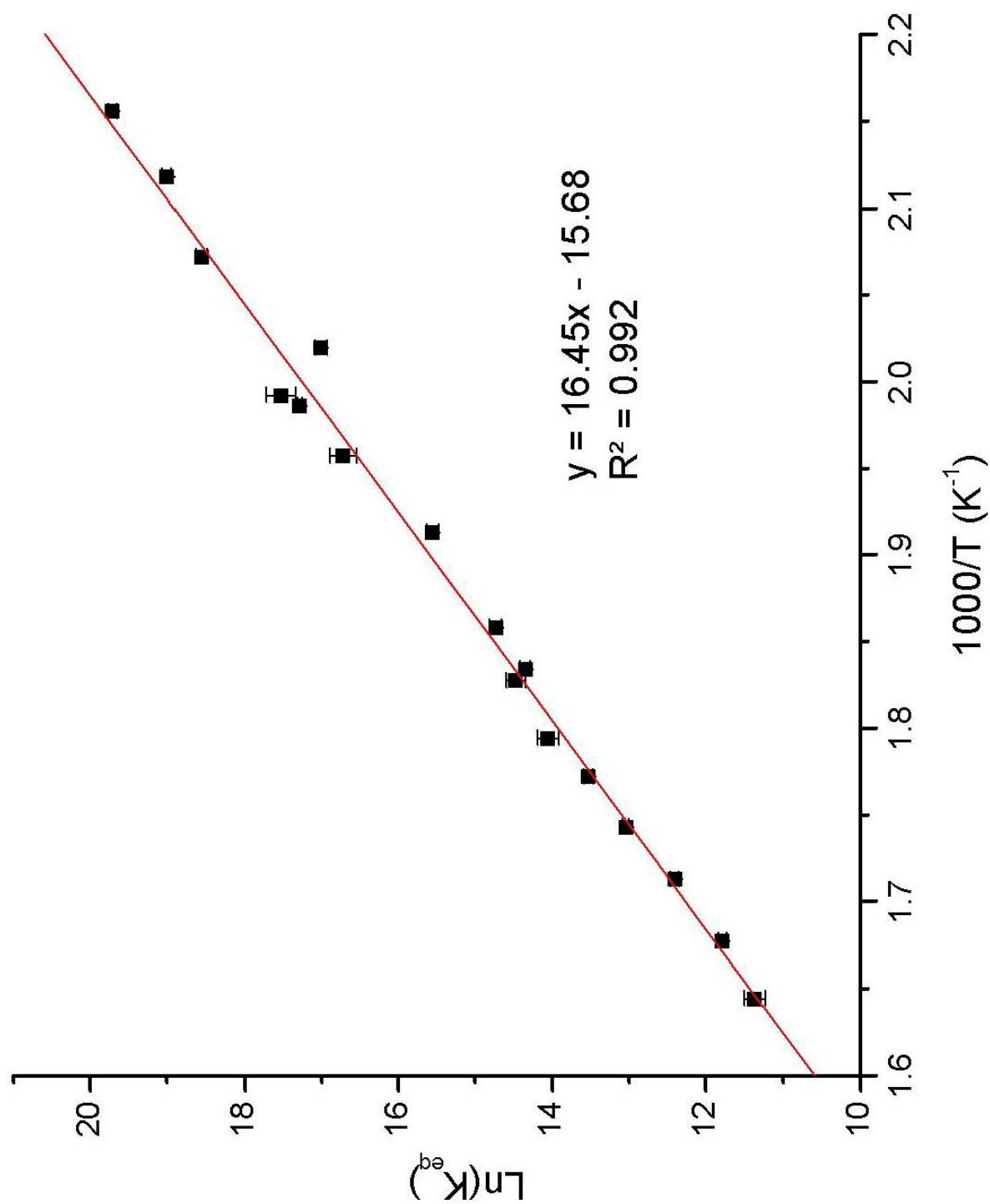


Figure 36 van't Hoff Plot of Na-Et₂O⁺

Electronic structure calculations were performed using a number of different methods. The calculation that agreed best with the experimental values used the B3LYP/6-311+G(d,p) method for geometry optimization and single point calculation. The calculated ΔH_{rxn} and ΔS_{rxn} are -126 kJ mol^{-1} and $-98 \text{ J mol}^{-1} \text{ K}^{-1}$ (Figure 38). Similiar results were obtained using different optimization methods and levels of theory. The results for the sodium-diethyether experiments and theory are tabulated in Table 9.

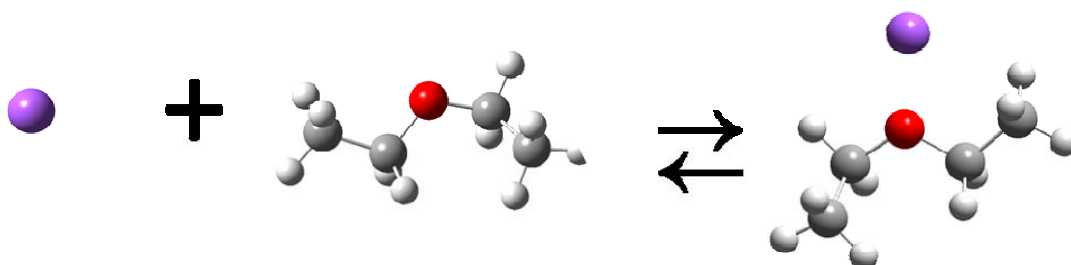


Figure 37 The B3LYP/6-311+G(d,p) Optimized Structure of Na-Et₂O⁺ Formation

Table 9 Na-Et₂O⁺ Thermochemical Data, Experimental and Calculated Summary

Source	ΔH (kJ mol ⁻¹) (kcal mol ⁻¹)	ΔS (J mol ⁻¹ K ⁻¹) (cal mol K ⁻¹)	ΔG (kJ mol ⁻¹) (kcal mol ⁻¹)
Current HPMS Experiment	-136.8 (-32.7)	-130.4 (-31.2)	-89.6 (-21.4)
Previous HPMS Experiment ⁷⁸	-130.0 (-31.1)	-118.0 (-28.2)	-94.8 (-22.7)
Previous ICR Experiment ⁷¹			-89.1 (-21.3)
B3LYP/ 6-311+G(d,p)	-125.6 (-30.0)	-97.6 (-23.3)	-96.5 (-23.1)
MP2(full)/ 6-311++G(2d,2p)	-122.2 (-29.2)	-98.4 (-23.5)	-92.9 (-22.2)
G3(MP2)	-118.0 (-28.2)	-92.0 (-22.0)	-90.6 (-21.6)
CBS-Q	-116.1 (-27.7)	-92.3 (-22.1)	-88.5 (-21.2)

The sodium-diethylether experiments proved to be challenging, even using the stainless steel boat as the sodium container. The average lifetime of the sodium was close to two weeks, however, significant time was required to achieve equilibrium inside the ion source each time the sodium sample required replenishment. The experimental ΔH_{rxn} is $-137 \pm 2.5 \text{ kJ mol}^{-1}$ which is somewhat removed from previous experimental and current theoretical determinations. The only other absolute measure of the binding energy of sodium cation to diethylether is by Guo et al., which reported a value of 130 kJ mol^{-1} .⁷⁸ All current calculations predict a weaker binding energy than both experimental values.

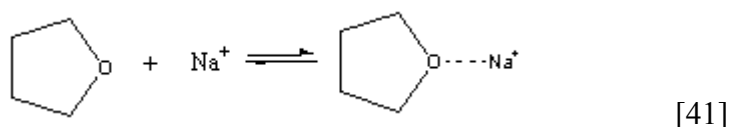
The entropy loss was consistent among current and previous HPMS experiments, with values of $-130 \pm 10 \text{ J mol}^{-1} \text{ K}^{-1}$ and $-118 \pm 10 \text{ J mol}^{-1} \text{ K}^{-1}$, respectively. All current theoretical entropy determinations result in a $\Delta S_{\text{rxn}} < 100 \text{ J mol}^{-1} \text{ K}^{-1}$. It appears that current calculated entropies of reaction are underestimating the entropy loss as both experimental values for the entropy change are in good agreement.

McMahon and Ohanessian used the ICR method to determine the Gibbs free energy change for the sodium-diethylether association reaction. They reported a value of $-89.1 \text{ kJ mol}^{-1}$ which is in very good agreement with all calculations performed.

4.3 THF Results and Discussion

4.31 Na-THF⁺ Measurement

The association reaction involving tetrahydrofuran (THF) and the sodium cation is in Eq. 41.



The reaction was observed over a temperature range of 193 to 339 °C, a 146 ° range. Depending on the temperature, between 1 and 50 μL of THF was injected into a heated 5 L stainless steel reservoir. The minimum injection volume amount for any solvent clustering gas is essentially 1 μL . It is difficult to accurately transfer a volume less than that using gas syringes and a 5 L reservoir. Further dilution of the solvent gas is achieved through a gas dilution. The clustering solvent (1 μL) is injected into a partially filled reservoir. The reservoir is then filled to a regular pressure (e.g. 1000 torr) and allowed to equilibrate with the solvent gas. Once equilibrium inside the reservoir is achieved the mixture is then reduced to a lower pressure (e.g. 100 torr). Since the gas mixture was in equilibrium and the total pressure of the system is reduced (by a factor of 10, in this case) then both partial pressures (clustering gas and bath gas) are also reduced by the same factor. In the example above, the 100 torr mixture remaining in the reservoir would essentially contain 0.1 μL of the clustering gas. The reservoir is then filled again (e.g. 1000 torr) and the resulting partial pressure of the clustering gas is ten times lower than the

original mixture. This process can be repeated if even a lower partial pressure of clustering gas is desired.

For a typical experiment the THF liquid is injected into the reservoir and allowed to equilibrate for thirty minutes. The gas mixture is then flowed into the ion source (if no gas dilutions are necessary) and allowed to react with the sodium vapour. The electronics are then turned on and allowed to equilibrate (≈ 15 minues) to allow for any electronic drift effects. Time-intensity profiles were collected for m/z 23 and 95 corresponding to the sodium cation and Na-THF^+ , respectively. A van't Hoff plot was generated over the 148 ° temperature range (Figure 39). Using Eq. 17 and 18 the enthalpy and entropy values of the association reaction were obtained. The enthalpy change was determined to be $-118.8 \pm 2.5 \text{ kJ mol}^{-1}$ and the entropy change was determined to be $-90.4 \pm 10 \text{ J mol}^{-1} \text{ K}^{-1}$.

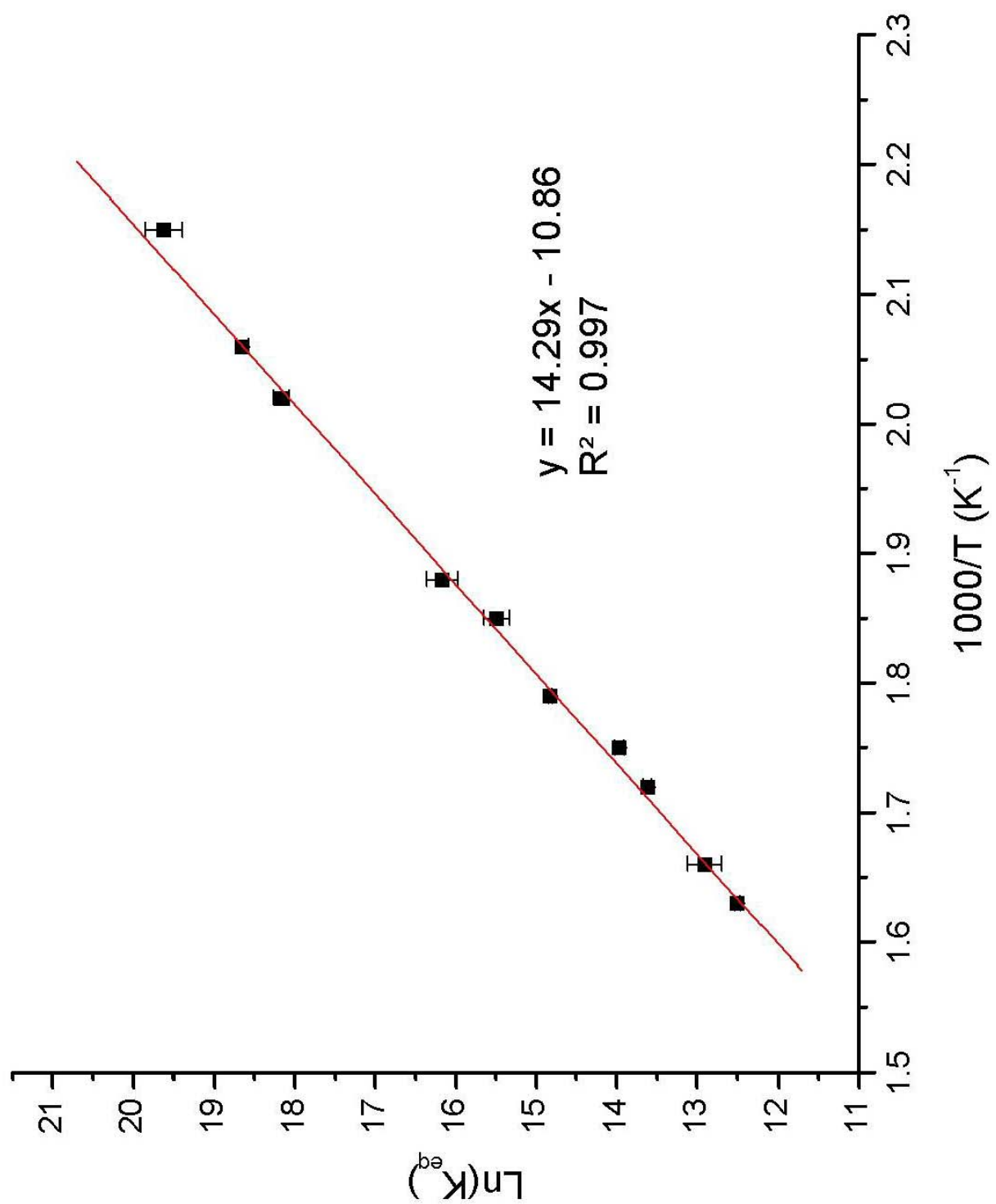


Figure 38 van't Hoff Plot of Na-THF⁺ Formation

Ab initio calculations were performed using the G3(MP2) compound method for geometry optimization and single point determination. The calculated ΔH_{rxn} and ΔS_{rxn} are -119 kJ mol^{-1} and $-100 \text{ J mol}^{-1} \text{ K}^{-1}$ (Figure 40). The results for the sodium-THF experiment and theory are tabulated below (Table 10). No other experimental data has been reported on the Na-THF^+ thermochemistry.

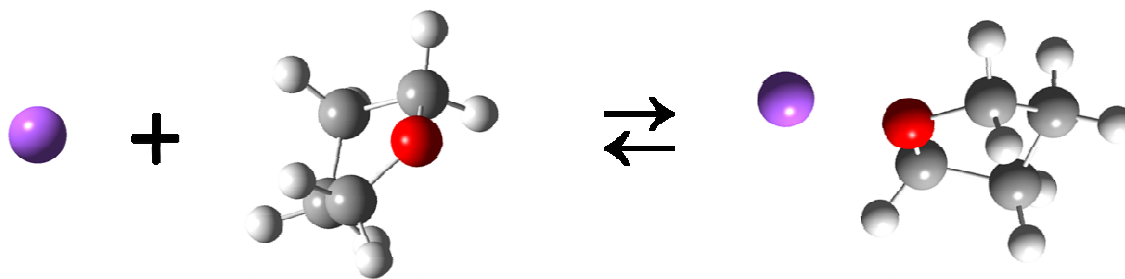


Figure 39 The G3(MP2) Optimized Structure of Na-THF^+ Formation

Table 10 Na-THF^+ Thermochemical Data, Experimental and Calculated Summary

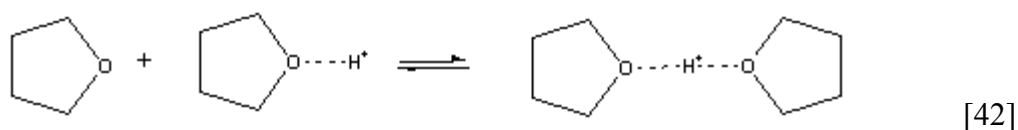
Source	$\Delta H \text{ (kJ mol}^{-1}\text{)}$ (kcal mol ⁻¹)	$\Delta S \text{ (J mol}^{-1} \text{ K}^{-1}\text{)}$ (cal mol K ⁻¹)	$\Delta G \text{ (kJ mol}^{-1}\text{)}$ (kcal mol ⁻¹)
Current HPMS Experiment	-118.8 (-28.4)	-90.4 (-21.6)	-91.8 (-22.0)
G3(MP2)	-119.0 (-28.4)	-100.0 (-23.9)	-89.1 (-21.3)

The values obtained from the van't Hoff plot for formation of the Na-THF^+ cluster are in very good agreement with the current theoretical calculations. The ΔH_{rxn} and ΔS_{rxn} obtained from the van't Hoff plot are $-118.8 \pm 2.5 \text{ kJ mol}^{-1}$ and $-90.4 \pm 10 \text{ J mol}^{-1} \text{ K}^{-1}$, respectively.

G3(MP2) calculations agree very well with the Na-THF^+ experimental data. The calculated enthalpy and entropy changes are -119 kJ mol^{-1} and $-100 \text{ J mol}^{-1} \text{ K}^{-1}$. Figure 40 appears to be an accurate description of the bonding that is occurring in the Na-THF^+ complex.

4.32 THF PBD Measurement

At the same times as the Na-THF⁺ experiments, THF PBD measurements were also carried out. The association reaction involving the formation of the PBD of tetrahydrofuran is given by Eq. 42.



The reaction was observed over nearly the same temperature range as the Na-THF⁺ system, 191 to 321 °C, a 148 ° temperature range. Depending on the temperature, between 1 and 50 μL of THF was injected into a heated 5 L stainless steel reservoir. For a typical experiment the THF liquid is injected into the reservoir and allowed to equilibrate for thirty minutes. The gas mixture is then flowed into the ion source. The electronics are then turned on and allowed to equilibrate (≈ 15 minues) to allow for any electronic drift effects. Time-intensity profiles were collected for m/z 73 and 143 corresponding to the protonated monomer and dimer of THF, respectively. A van't Hoff plot was generated over the 148 ° temperature range (Figure 41). Using Eq. 17 and 18 the enthalpy and entropy values of the association reaction were obtained. The enthalpy change was determined to be $-124 \pm 2.5 \text{ kJ mol}^{-1}$ and the entropy change was determined to be $-121 \pm 10 \text{ J mol}^{-1} \text{ K}^{-1}$.

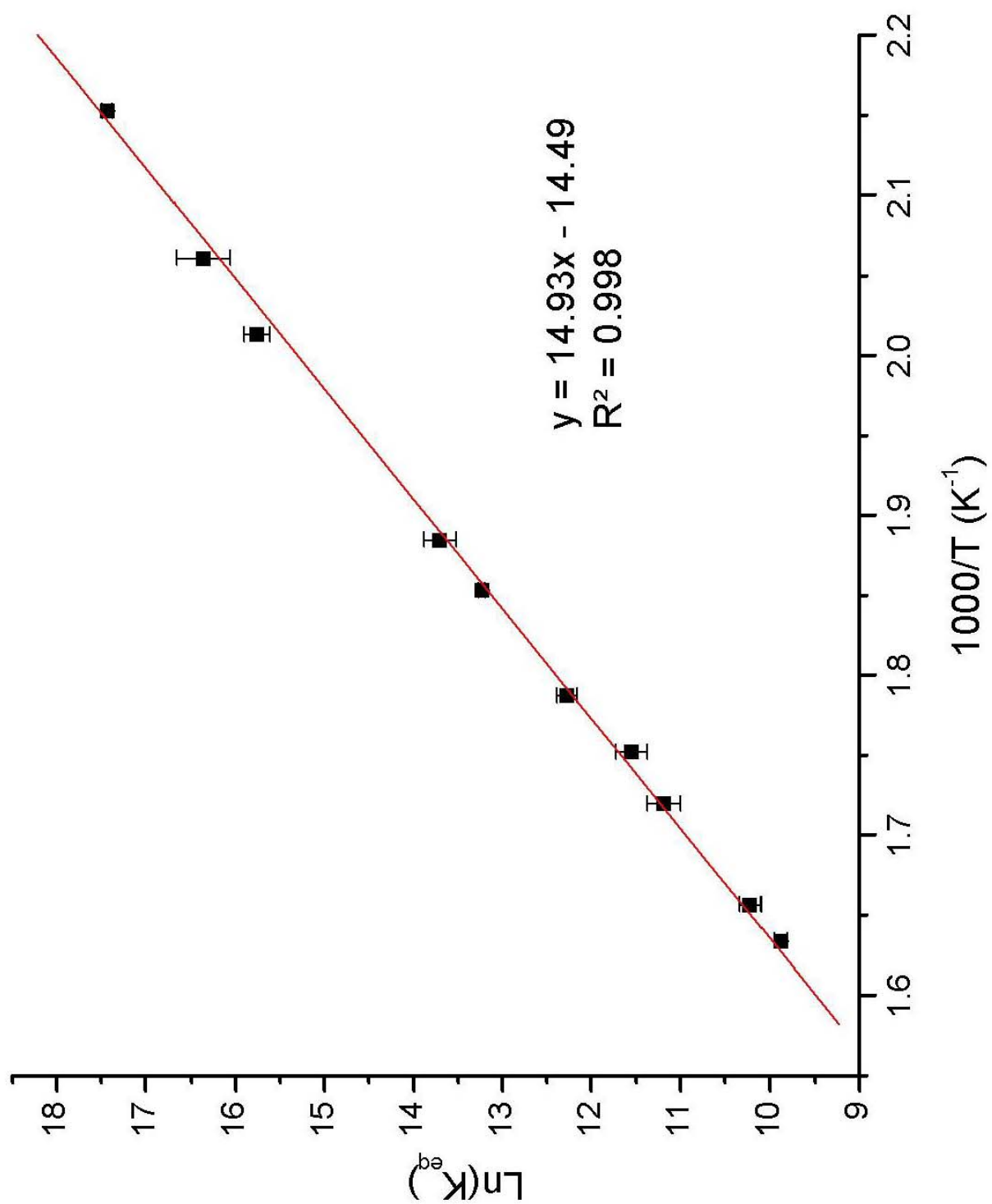


Figure 40 van't Hoff Plot of THF PBD Formation

Ab initio calculations were performed using the G3(MP2) compound method for geometry optimization and single point determination. The calculated ΔH_{rxn} and ΔS_{rxn} are -131 kJ mol⁻¹ and -130 J mol⁻¹ K⁻¹ (Figure 42). The results for the THF PBD experiment and theory are tabulated below (Table 11).

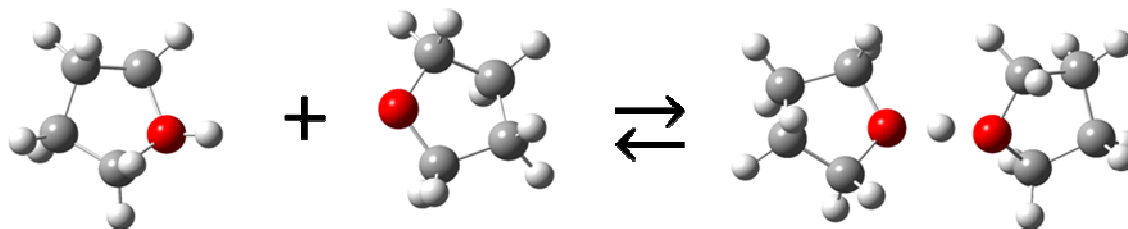


Figure 41 The G3(MP2) Optimized Structure of THF PBD Formation

Table 11 THF PBD Thermochemical Data, Experimental and Calculated Summary

Source	ΔH (kJ mol ⁻¹) (kcal mol ⁻¹)	ΔS (J mol ⁻¹ K ⁻¹) (cal mol K ⁻¹)	ΔG (kJ mol ⁻¹) (kcal mol ⁻¹)
Current HPMS Experiment	-124.1 (-29.7)	-120.5 (-28.8)	-88.2 (-21.1)
Previous HPMS Experiment ⁷⁹	-125.1 (-29.9)	-121.8 (-29.1)	-88.8 (-21.2)
G3(MP2)	-130.8 (-31.3)	-130.2 (-31.1)	-92.0 (-22.0)

The values obtained from the van't Hoff plot for formation of the THF PBD are in good agreement with the current theoretical calculations. The ΔH_{rxn} and ΔS_{rxn} obtained from the van't Hoff plot are -124.1 ± 2.5 kJ mol⁻¹ and -120.5 ± 10 J mol⁻¹ K⁻¹, respectively. Hiraoka et al. also investigated the THF PBD system and obtained very similar values.⁷⁹ G3(MP2) calculations agree fairly well with the experimental values. The binding energy predicted by the G3(MP2) theory seems to slightly overestimate the strength of the IHB, however, Figure 42 appears to be an accurate description of the bonding occurring during the THF PBD formation.

4.4 *Conclusion*

A new method for sodium ion production in high-pressure mass spectrometry environments has been accomplished. Sodium ion measurements are now possible below 150°C.

Sodium bound complexes have been investigated using diethyl ether and tetrahydrofuran as ligands. The experimental binding energy of the sodium-diethylether complex is slightly higher than previous experiment and current calculations. The sodium-tetrahydrofuran binding energy is in very good agreement with current calculations. The tetrahydrofuran proton bound dimer formation was also found to be in good agreement with previous experimental and current theoretical data. CP-dG2thaw, a relatively new theory for calculations involving molecules and molecular ions containing one or metal ions, appears to be adequate for systems involving the sodium cation.

5.0 References

- (1) Fridgen, T. D.; McMahon, T. B.; MacAleese, L.; Lemaire, J.; Maitre, P. *J. Phys. Chem. A* **2004**, *108*, 9008.
- (2) Wentworth, P. J.; Nieva, J.; Takeuchi, C.; Galve, R.; Wentworth, A. D.; Dilley, R. B.; DeLaria, G. A.; Saven, A.; Baboir, B. M.; Janda, K. D.; Eschenmoser, A.; Lerner, R. A. *Science* **2003**, *302*, 1053.
- (3) Hartquist, T. W.; Williams, D. A. *The Chemically Controlled Cosmos: Astronomical Molecules from the Big Bang to Exploding Stars*; Cambridge University Press: New York, 1995.
- (4) Lias, S. G.; Bartmess, J. E. Gas-Phase Ion Thermochemistry. In *NIST Chemistry WebBook*; Mallard, W. G., Linstrom, P. G., Eds.; NIST Standard Reference Database Number 69; National Institute of Standards and Technology: Gaithersburg, MD, August 2007 (<http://webbook.nist.gov>)
- (5) McMahon, T. B. High Pressure Mass Spectrometry. In *Energetics of Stable Molecules and Reactive Intermediates*; Minas da Piedade, M. E., Ed.; Kluwer Academic Publishers: Netherlands, 1999; pp 259.
- (6) Kebarle, P.; Godbole, E. W. *J. Chem. Phys.* **1962**, *36*, 302.
- (7) Kebarle, P. *Ann. Rev. Phys. Chem.* **1977**, *28*, 445.
- (8) Aue, H. D.; Bowers, M. T. Stabilities of positive ions from equilibrium gas-phase basicity measurements. In *Gas Phase Ion Chemistry*; Bowers, M. T., Ed.; Academic Press: New York, 1979; Vol. 2; pp 2.
- (9) Meot-Ner, M. *Chem. Rev.* **2005**, *105*, 213.
- (10) Gamble, T. N. Deuterium Isotop Effects on the Energetics of Clustering Reactions for Small Organic Ions, University of Waterloo, 2000.
- (11) Wincel, H. *Chemical Phys. Lett.* **2007**, *439*, 157.
- (12) McMahon, T. B. Experimental Approaches to the Unimolecular Dissociation of Gaseous Cluster Ions. In *Advances in Gas-Phase Ion Chemistry*; Adams, N. B., Babcock, L. M., Eds.; JAI: Greenwich, CT, 1996; Vol. 2; pp 41.
- (13) Olah, G. A.; Prakash, G. K. S.; Sommer, J. *Superacids*; John Wiley & Sons: Toronto, 1985; Vol. 1.
- (14) Szulejko, J. E.; McMahon, T. B. *Int. J. Mass Spec. Ion Proc.* **1991**, *109*, 279.
- (15) Foresman, J. B.; Frisch, A. E. *Exploring Chemistry with Electronic Structure Methods*, 2nd ed.; Gaussian, Inc.: Pittsburgh, PA, 1996.
- (16) Møller, C.; Plesset, M. S. *Phys. Rev.* **1934**, *4*, 618.
- (17) Zeigker, T. *Can. J. Chem.* **1999**, *73*, 743.
- (18) Raymond, K. S.; Wheeler, R. A. *J. Comp. Chem.* **1999**, *20*, 207.
- (19) Mó, O.; Yáñez, M.; Decouzon, M.; Gal, J. F.; Maria, P. C.; Guillemin, J. C. *J. Am. Chem. Soc.* **1999**, *121*, 4653.
- (20) McLean, A. D.; Chandler, G. S. *J. Chem. Phys.* **1980**, *72*, 5639.
- (21) Krishnan, R.; Binkley, J. S.; Seeger, R.; Pople, J. A. *J. Chem. Phys.* **1980**, *72*, 650.

- (22) Frisch, M. J.; Pople, J. A.; Binkley, J. S. *J. Chem. Phys.* **1984**, *80*, 3265.
- (23) Clark, T.; Chandrasekhar, K.; Spitznagel, G. W.; Schleyer, P. v. R. *J. Comp. Chem.* **1983**, *4*, 294.
- (24) Curtiss, L. A.; Raghavachari, K. G2 Theory. In *The Encyclopedia of Computational Chemistry*; Schleyer, P. v. R., Ed.; John Wiley & Sons Ltd: Athens, USA, 1998; Vol. 2; pp 1104.
- (25) Curtiss, L. A.; Redfern, P. C.; Raghavachari, K.; Rassolov, V.; Pople, J. A. *J. Chem. Phys.* **1999**, *1999*, 4703.
- (26) Koné, M.; Illien, B.; Graton, J.; Laurence, C. *J. Phys. Chem. A* **2005**, *109*, 11907.
- (27) Frisch, M. J. T., G. W.; Schlegel, H. B.; Scuseria, G. E.; Robb, M. A.; Cheeseman, J. R.; Montgomery, Jr., J. A.; Vreven, T.; Kudin, K. N.; Burant, J. C.; Millam, J. M.; Iyengar, S. S.; Tomasi, J.; Barone, V.; Mennucci, B.; Cossi, M.; Scalmani, G.; Rega, N.; Petersson, G. A.; Nakatsuji, H.; Hada, M.; Ehara, M.; Toyota, K.; Fukuda, R.; Hasegawa, J.; Ishida, M.; Nakajima, T.; Honda, Y.; Kitao, O.; Nakai, H.; Klene, M.; Li, X.; Knox, J. E.; Hratchian, H. P.; Cross, J. B.; Bakken, V.; Adamo, C.; Jaramillo, J.; Gomperts, R.; Stratmann, R. E.; Yazyev, O.; Austin, A. J.; Cammi, R.; Pomelli, C.; Ochterski, J. W.; Ayala, P. Y.; Morokuma, K.; Voth, G. A.; Salvador, P.; Dannenberg, J. J.; Zakrzewski, V. G.; Dapprich, S.; Daniels, A. D.; Strain, M. C.; Farkas, O.; Malick, D. K.; Rabuck, A. D.; Raghavachari, K.; Foresman, J. B.; Ortiz, J. V.; Cui, Q.; Baboul, A. G.; Clifford, S.; Cioslowski, J.; Stefanov, B. B.; Liu, G.; Liashenko, A.; Piskorz, P.; Komaromi, I.; Martin, R. L.; Fox, D. J.; Keith, T.; Al-Laham, M. A.; Peng, C. Y.; Nanayakkara, A.; Challacombe, M.; Gill, P. M. W.; Johnson, B.; Chen, W.; Wong, M. W.; Gonzalez, C.; and Pople, J. A.; Gaussian 03, Revision C.02; Gaussian, Inc.: Wallingford CT, 2004.
- (28) Dennington II, R. K., Todd; Millam, John; Eppinnett, Ken; Hovell, W. Lee; Gilliland, Ray. Gaussview, Version 3.00; Semichem, Inc.: Shawnee Mission, KS, 2003.
- (29) Hoyau, S.; Norrman, K.; McMahon, T. B.; Ohanessian, G. *J. Am. Chem. Soc.* **1999**, *121*, 8864.
- (30) Borgstedt, H. U.; Mathews, C. K. *Applied Chemistry of the Alkali Metals*; Plenum Press: New York, 1987.
- (31) Alcock, N. W. *Bonding and Structure: Structural Principles in Inorganic and Organic Chemistry*; Ellis Horwood: New York, 1990.
- (32) Atkins, P. W. *Physical Chemistry*, 6th ed.; W.H. Freeman and Company: New York, 2000.
- (33) Wenthold, P. G.; Squires, R. R. *J. Phys. Chem.* **1995**, *99*, 2002.
- (34) Aakeroy, C. B.; Beatty, A. M. *Aust. J. Chem.* **2001**, *54*, 409.
- (35) Tobita, S.; Tajima, S.; Suzuki, S.; Imamura, T.; Koyano, I. *Int. J. Mass Spec. Ion Proc.* **1991**, *105*, 101.
- (36) Meot-Ner, M. *J. Am. Chem. Soc.* **1983**, *105*, 4906.
- (37) Lowery, A. H.; George, C.; Antonia, P. D.; Karle, J. *J. Am. Chem. Soc.* **1971**, *93*, 6399.
- (38) Brown, R. S.; Nakashima, A. T.; Haddon, R. C. *J. Am. Chem. Soc.* **1979**, *101*, 3175.
- (39) Emsley, J. *Structure and Bonding*; Springer: Berlin, 1984; Vol. 2.
- (40) Hibbert, F.; Emsley, J. Hydrogen Bonding and Chemical Reactivity. In *Advances in Physical Chemistry*; Academic Press: London, 1990; Vol. 26.
- (41) Bouchoux, G. *Mass Spec. Rev.* **1988**, *7*, 203.
- (42) Keffe, J. R.; Kresge, A. J. *The Chemistry of Enols*; Wiley: New York, 1990.
- (43) Caravatti, P.; Allemann, M. *Org. Mass Spec.* **1991**, *26*, 514.

- (44) Bouchoux, G. *Mass Spec. Rev.* **1988**, 7, 1.
- (45) Bertrand, W.; Bouchoux, G. *Rapid Commun. Mass Spec.* **1998**, 12, 1697.
- (46) van der Rest, G.; Nedev, H.; Chamot-Rooke, J.; Mourgues, P.; McMahon, T. B.; Audier, H. E. *Int. J. Mass Spec.* **2000**, 202, 161.
- (47) Hudlicky, M. *Chemistry of organic fluorine compounds*; MacMillan: New York, 1962.
- (48) Sheppard, W. A.; Sharts, C. M. *Organic Fluorine Chemistry*; Benjamin: New York, 1969.
- (49) Doiron, C. E.; McMahon, T. B. *Can. J. Chem.* **1981**, 59, 2689.
- (50) Faird, R.; McMahon, T. B. *Can. J. Chem.* **1980**, 58, 2307.
- (51) Drummond, D. F.; McMahon, T. B. *J. Phys. Chem.* **1981**, 85, 3746.
- (52) Drummond, D. F.; McMahon, T. B. *Int. J. Mass Spec. Ion Physics* **1982**, 42, 265.
- (53) Bassetti, M.; Cerichelli, G.; Floris, B. *Tetrahedron* **1988**, 44, 2997.
- (54) Bassetti, M.; Cerichelli, G.; Floris, B. *Gazz. Chim. Ital.* **1986**, 116, 579.
- (55) Tollec, J. In *The Chemistry of Enols*; Rappoport, Z., Ed.; John Wiley & Sons, Inc.: New York, 1990.
- (56) Lintvedt, R. L.; Holtzclaw, J. *J. Am. Chem. Soc.* **1966**, 88, 2713.
- (57) Henry, M. C.; Yonker, C. R. *Anal. Chem.* **2004**, 76, 4684.
- (58) Zahedi-Tabrizi, M.; Tayyari, F.; Moosavi-Tekyeh; Jalali, A.; Tayyari, S. F. *Spectrochimica Acta A* **2006**, 65, 387.
- (59) Hoffman, T. L. The Effects of Size and Functionality on Zero-Pressure Thermal-Radiation-Induced Dissociation, Univeristy of Waterloo, 1997.
- (60) Larson, J. W.; McMahon, T. B. *J. Am. Chem. Soc.* **1982**, 104, 6255.
- (61) Silverstein, R. M.; Webster, F. X. *Spectrometric Identification of Organic Compounds*, 6th ed.; John Wiley & Sons, Inc.: New York, 1998.
- (62) Emsley, J.; Freeman, N. J. *J. Mol. Struc.* **1987**, 161, 193.
- (63) Buemi, G. *J. Mol. Struc.* **2000**, 499, 21.
- (64) Lippard, S. J.; Berg, J. M. *Principles of Bioinorganic Chemistry*; University Science Books: Mill Valley, CA, 1994.
- (65) Liao, P. C.; Allison, J. *J. Mass Spec.* **1995**, 30, 408.
- (66) Zhang, J.; Knochenmuss, R.; Stvenson, E.; Zenobi, R. *Int. J. of Mass Spec.* **2002**, 213, 237.
- (67) Wytttenbach, T.; Bowers, M. T. *Annu. Rev. Phys. Chem.* **2007**, 58, 511.
- (68) Dunbar, R. C.; Petrie, S. *Astrophys. J.* **2002**, 564, 792.
- (69) Petrie, S.; Dunbar, R. C. *J. Phys. Chem. A* **2000**, 104, 4480.
- (70) Hoyau, S.; Norrman, K.; McMahon, T. B.; Ohanessian, G. *J. Am. Chem. Soc.* **1999**, 121, 8864.
- (71) McMahon, T. B.; Ohanessian, G. *Chem. Eur. J.* **2000**, 6, 2931.
- (72) Armentrout, P. B.; Rodgers, M. T. *J. Phys. Chem. A* **2000**, 104, 2238.
- (73) Rodgers, M. T.; Armentrout, P. B. *Mass Spec. Rev.* **2000**, 19, 215.
- (74) Amicangelo, J. C.; Armentrout, P. B. *Int. J. Mass Spec.* **2001**, 212, 301.
- (75) Petrie, S. *J. Phys. Chem. A* **2001**, 105, 9931.
- (76) Petrie, S.; Gatt, P.; Davies, E.; Bloomfield, J. *J. Phys. Chem. A* **2006**, 110, 1134.
- (77) Curtiss, L. A.; Carpenter, J. E.; Raghavachari, K.; Pople, J. A. *J. Chem. Phys.* **1991**, 94, 7221.
- (78) Guo, B. C.; Conklin, B. J.; Castleman, A. W. *J. Am. Chem. Soc.* **1989**, 111, 6506.
- (79) Hiraoka, K.; Takimoto, H.; Yamabe, S. *J. Phys. Chem.* **1986**, 90, 5910.